AFRL-AFOSR-VA-TR-2020-0134

Quantification of Microstructurally Short Crack Growth in Superalloys

Anthony Rollett
CARNEGIE MELLON UNIVERSITY

07/22/2020
Final Report

Air Force Research Laboratory
AF Office Of Scientific Research (AFOSR)/ RTA1
Arlington, Virginia 22203
Air Force Materiel Command

DISTRIBUTION A: Distribution approved for public release.

REPORT DOCUMENTATION PAGE

Form Approved
OMB No. 0704-0188

1. REPORT DATE *(DD-MM-YYYY)*	2. REPORT TYPE	3. DATES COVERED *(From - To)*
13-08-2020	Final Performance	01 Jan 2016 to 31 Dec 2019

4. TITLE AND SUBTITLE
Quantification of Microstructurally Short Crack Growth in Superalloys

5a. CONTRACT NUMBER

5b. GRANT NUMBER
FA9550-16-1-0105

5c. PROGRAM ELEMENT NUMBER
61102F

6. AUTHOR(S)
Anthony Rollett

5d. PROJECT NUMBER

5e. TASK NUMBER

5f. WORK UNIT NUMBER

7. PERFORMING ORGANIZATION NAME(S) AND ADDRESS(ES)
CARNEGIE MELLON UNIVERSITY
5000 FORBES AVENUE
PITTSBURGH, PA 15213-3815 US

8. PERFORMING ORGANIZATION REPORT NUMBER

9. SPONSORING/MONITORING AGENCY NAME(S) AND ADDRESS(ES)
AF Office of Scientific Research
875 N. Randolph St. Room 3112
Arlington, VA 22203

10. SPONSOR/MONITOR'S ACRONYM(S)
AFRL/AFOSR RTA1

11. SPONSOR/MONITOR'S REPORT NUMBER(S)
AFRL-AFOSR-VA-TR-2020-0134

12. DISTRIBUTION/AVAILABILITY STATEMENT
A DISTRIBUTION UNLIMITED: PB Public Release

13. SUPPLEMENTARY NOTES

14. ABSTRACT
Based on characterization of Ti-7Al using High Energy Diffraction Microscopy (HEDM) at the Cornell High Energy Synchrotron Source, new information was obtained on a) temperature- dependent anisotropic thermal expansion, b) evolution of micro-mechanical state at the grain scale under cyclic loading, c) sensitivity of results from far field-HEDM to analysis variables and d) evaluation of RVE size with respect to micromechanics and crystallographic texture.

15. SUBJECT TERMS
crack growth, fatigue, computed tomography

16. SECURITY CLASSIFICATION OF:			17. LIMITATION OF ABSTRACT	18. NUMBER OF PAGES	19a. NAME OF RESPONSIBLE PERSON
a. REPORT	b. ABSTRACT	c. THIS PAGE			TILEY, JAIMIE
Unclassified	Unclassified	Unclassified	UU		19b. TELEPHONE NUMBER *(Include area code)* 703-588-8316

Standard Form 298 (Rev. 8/98)
Prescribed by ANSI Std. Z39.18

Final Report to AFOSR for 2019

Quantification of Microstructurally Short Crack Growth in Superalloys

Grant Number: FA9550-16-1-0105

April 16, 2020

Principal Investigator:
Prof. Anthony D. Rollett[1]

Co-Principal Investigator:
Prof. Robert M. Suter[1]

Collaborators:
Rachel E. Lim[1], Dr. Darren C. Pagan[2], Dr. Paul A. Shade[3], Donald E. Boyce[4], Dr. Joel V. Bernier[5]

[1] *Carnegie Mellon University*,
[2] *Cornell High Energy Synchrotron Source*,
[3] *Air Force Research Laboratory*,
[4] *Cornell University*,
[5] *Lawrence Livermore National Laboratory*

Abstract

Based on characterization of Ti-7Al using High Energy Diffraction Microscopy (HEDM) at the Cornell High Energy Synchrotron Source, new information was obtained on a) temperature-dependent anisotropic thermal expansion, b) evolution of micro-mechanical state at the grain scale under cyclic loading, c) sensitivity of results from far field-HEDM to analysis variables and d) evaluation of RVE size with respect to micromechanics and crystallographic texture.

Summary for Year 4 (2019)

The fourth year of the project included continuing analysis of the data collected in prior years with an emphasis on preparing results for publication. The planned journal articles will be as follows:

- R.E. Lim, D.C. Pagan, D.E. Boyce, P.A. Shade, J.V. Bernier, A.D. Rollett, *Temperature-Dependent Anisotropy in Hexagonal Ti-7Al Revealed by Grain-Resolved Synchrotron Diffraction*, (In Preparation).
- R.E. Lim, D.C. Pagan, D.E. Boyce, P.A. Shade, J.V. Bernier, Y. Shen, R.M. Suter, A.D. Rollett, *Micromechanical Evolution of Ti-7Al Under Cyclic Loading.*
- R.E. Lim, J.V. Bernier, A.D. Rollett, P.A Shade, *Sensitivity Analysis of ff-HEDM Measurements.*
- R.E. Lim, M.J. Wilkin, J.G. Pauza, A.D. Rollett, *Using Distance Metrics to Evaluate 3D RVE Size for Micromechanics and Texture.*

Summary for Year 3 (2018)

The third year of the project included new x-ray work done at both the Advanced Photon Source (APS) at the Argonne National Lab. and the Cornell High Energy Synchrotron Source (CHESS). The experiment at CHESS acquired data on thermal expansion in Ti-7Al. This was aimed at resolving substantial uncertainty in the literature on the CTE of Ti and to enable hypotheses to be tested as to the origin of the state of residual elastic strain found in nominally fully annealed metals. Rachel Lim spent the Fall semester at AFRL with Dr. Paul Shade and developed a systematic sensitivity analysis for the far field HEDM reconstruction method; this showed, e.g., that the center-of-mass (of a grain) is much more sensitive to its distance from the center of rotation. The experiment at APS was a high speed (kHz) at beamline 1-ID and represented an opportunity to apply the knowledge of diffraction analysis acquired in this project to laser melting experiments. This showed that carbide and Laves phases appear almost immediately after solidification of Inconel 718.

Summary for Year 2 (2017)

In the second year of the project, we worked at both APS and at CHESS. In experiments in March 2017 at beamline 1-ID at APS, we acquired data from a deliberately voided sample of Ti-7Al, and worked with the PUP program headed up by Dr. Paul Shade (AFRL). In an experiment at beamline F2 at CHESS in June 2017, we worked with Dr. Darren Pagan to perform a cyclic deformation experiment on Ti-7Al. The results from the latter experiment are described in detail here and show several interesting trends in terms of stress and strain, and the progression of the macroscopic stress-strain curve for the cyclic loading appears to provide evidence for sub-yield ratcheting (Fig. 1.6). There is also evidence that a small minority of grains undergo microplastic events as evidenced by changes in their elastic strain

state (Fig. 1.11) and in their crystallographic orientation (Fig. 1.12). The FFT method was used to simulate the experiment, which showed good agreement in general but the ratcheting together with the microplasticity was not well captured.

Summary for Year 1 (2016)

The first year of the project demonstrated our ability to model the elastic response of a polycrystalline sample of Ti-7Al based on a previous collaborative experiment using the FFT-based MASSIF code. In December 2016, we conducted our first experiment at beamline 1-ID of APS in which we applied cyclic loading to Ti-7Al. The switch from the superalloys originally proposed was based on a close collaboration with a team of researchers from the RX division of AFRL, led by Dr. Paul Shade. Preliminary analysis of the results indicated many interesting changes in the strain state of individual grains.

People

The PI for the project is Prof. Anthony (Tony) D. Rollett in the Materials department, with co-PI Robert M. Suter in the Physics department. In the second year, Rachel Lim (US citizen) was supported on the project. As noted previously, the project is being conducted in close collaboration with Drs. Paul Shade, William Musinski, and Adam Pilchak of the RX division of AFRL at the Wright-Patterson Air Force Base (WPAFB).

Materials

The title of the project indicates that the project would focus on microstructurally short cracks in superalloys. However, our collaboration with AFRL has re-focused the work on a research alloy, Ti-7Al, which has received a good deal of attention in the joint experiments between AFRL, Carnegie Mellon University (specifically, Robert Suter), Lawrence Livermore National Lab. (Joel Bernier), and the beam line scientists at APS, specifically beamline 1-ID. Cracks have been observed before in this material, but the response of the material has not been investigated, and especially not the response under cyclic loading. It has also been the material that was used exclusively for experiments under a Partner User Project (PUP) that was the formal vehicle for the collaboration mentioned above. The PUP has mainly used High Energy Diffraction Microscopy to measure orientation maps and elastic strain state in the Ti-7Al. The co-PI on this project, Robert Suter, has also been a key participant in the PUP through his development of the near field high energy diffraction microscopy (nf-HEDM) method.

Sensitivity Analysis of Experimental Parameters on Far-Field HEDM Measurements

Rachel E. Lim, Joel V. Bernier, Anthony D. Rollett, Paul A. Shade

1.1 Introduction

Techniques for the study of microstructure and micromechanics of materials in 3D have developed rapidly over the past 20 years. In particular, the use of synchrotron light sources allows for the non-destructive study of the evolution of materials *in situ*. One of these techniques, far-field high-energy x-ray diffraction microscopy (ff-HEDM), is being used to track mesoscale strain evolution in polycrystals.

In 2011, Edmiston et al [1], studied the precision uncertainty in lattice strain and orientation measurements using high-energy monochromatic X-ray diffraction. In the work, it was specified that they were "specifically addressing precision uncertainty [2], that is, we regard the effect of errors considered to be random in nature, and do not provide dedicated analysis of accuracy or bias error. Bias errors will be largely dependent upon the experimental equipment and setup used in each individual case..." This bias error from experimental equipment and setup and its effects on the calculated center-of-mass (COM), grain-averaged orientation, and grain-averaged elastic strain tensor was studied in the work done here.

In 2011, Schuren & Miller [3] studied the strain uncertainty coming from the instrument (detector) and from the material. One major factor they looked at was the effect of azimuthal binning into pixels.

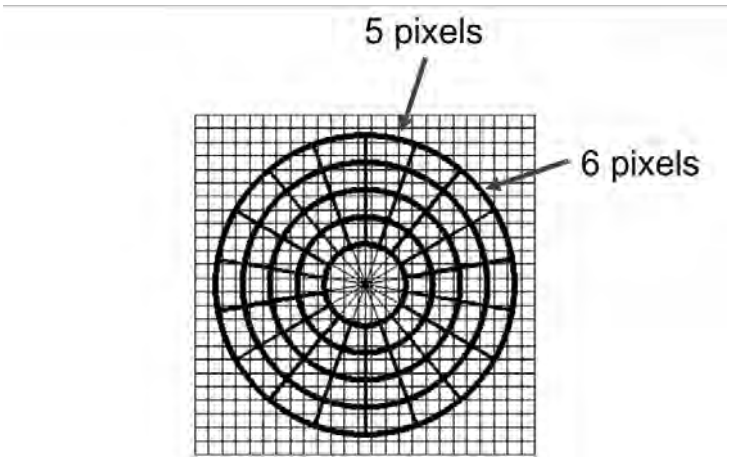

Figure 1.1: The top bin only covers five pixels while the top right bin covers 6 pixels.

1.1.1 Known Sources of Error

There are several other known sources of error in ff-HEDM data reduction that will not be considered here. The first is the effects of detector calibration. Renversade et al [4] stated that "the error of normal strain components (about 1×10^{-4}) is mainly caused by calibration errors, while the error of shear components (about 0.5×10^{-4}) is largely influenced by counting statistics and random spot-centre errors due to detector distortion."

Another source of error comes from the flyscanning method that is used to take data. The sample is continuously rotated through omega, so each frame actually covers an omega range, not just the one omega value. Thus, we do not know what the exact omega value for a diffraction peak is. For example, in Figure 1.1.1, for a 0.25° frame extending from $\omega = 0°$ to $\omega = 0.25°$, the peak could land at 1, 2, or 3, but would all be counted in the same frame, so the only information would be that the peak lands between 0° and 0.25°

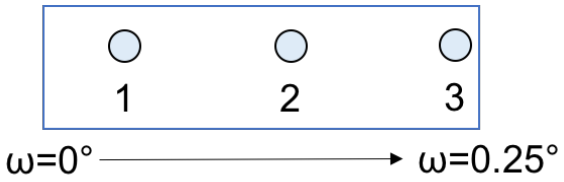

Figure 1.2: There is significantly less resolution in omega because for a single frame, an x-ray peak could land at 1, 2, or 3 within the omega range, and there is no way to know where exactly it landed.

A different source of error comes from the way peaks are found for fitting the twelve grain parameters (3 COM, 3 orientation, 6 strain tensor). Tolerances in 2θ, η, and ω are defined in the configuration file for grain fitting which describe the size of the box drawn around the predicted peak location. A tight box can be drawn around peaks for grains with little orientation spread (Fig. 1.3a) while a larger box needs to be drawn around peaks for grains with more orientation spread. If the box is drawn too large, specifically in polycrystals, it is likely that multiple peaks will land inside the box, and there is no way to know which peak is the correct one. If the box is drawn too tight, it will not fit entirely within the box (Fig. 1.3b).

1.2 Methodology

1.2.1 Variables

A diffraction simulator was developed to model the experimental setup with the variety of different parameters shown in Table 1.1. Using this diffraction simulator, we hope to be able to find the best set of parameters to use for a given material and experiment. For example, metals with higher atomic numbers such as nickel or iron require higher energies to be used to get full x-ray penetration. Also, if orientation resolution is less important, a larger rotation step size could possibly be used which would speed up experiments. In addition to finding the best experimental setup, this diffraction simulator

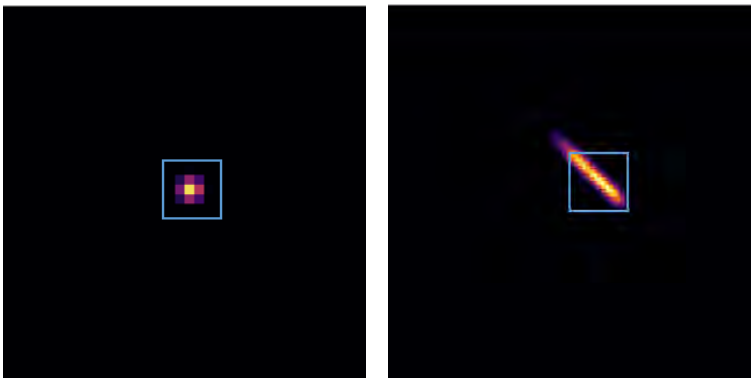

(a) Ruby peak (b) Deformed gold peak

Figure 1.3: A box drawn around (a) a tight peak will likely not work for (b) a deformed peak, and the fitting algorithm is sensitive to this.

can be used to study which parameters more strongly affect the experimental resolution. Currently most of the understanding into bias error comes from observation and experience rather than a thorough study.

Variable Set	Variables	Values or Range of Values
Energy	Nominal Energy	55.615, 61.331, 65.350, 71.677, 80.726 (keV)
Energy	Energy Bandpass	High-Energy Mono, High-Res Mono
Detector	Number of Detectors	1, 2, 4
Detector	Detector Distance	0.5-2 m (depending on number of detectors)
Detector	Pixel Size	74.8×74.8, 200×200 (μm^2)
Rotation	Rotation Range	180°, 360°
Rotation	Rotation Step Size	0.25°, 0.5°, 1.0°
Two Theta	Max 2θ Reconstructed	4, 6, 8, 10 (rings)

Table 1.1: A variety of different experimental parameters were included as variable inputs for the diffraction simulator.

The two biggest variables that are being studied are the detector parameters (number of detectors, detector distance, and pixel size) and the rotation parameters (rotation range and rotation step size). At APS, there are currently two possible detector setups. There is a choice of using a single GE detector (Fig. 1.4a), that is 2048×2048 pixels with a pixel size of 200 μm, or four GE detectors had be placed in the "hydra" setup (Fig. 1.4c). At CHESS, the current default setup is two Dexela detectors, with 3889×3073 pixels with a pixel size of 74.8 μm, placed side-by-side (Fig. 1.4b).

1.2.2 Diffraction Simulator and Reduction

A diffraction simulator and reduction algorithm was formulated where the physical experiment is first initialized with the instrument and material parameters. Then all the other parameters of interest are initialized such as the energy and rotation range and step size. The rotation series is simulated which calculates the diffraction vectors in terms of 2θ, η, and ω for the all of the orientations of interest. For each diffraction vector, the omega value is binned into the appropriate frame depending on the omega step size chosen. The intersection between the diffraction vector and detector is calculated in

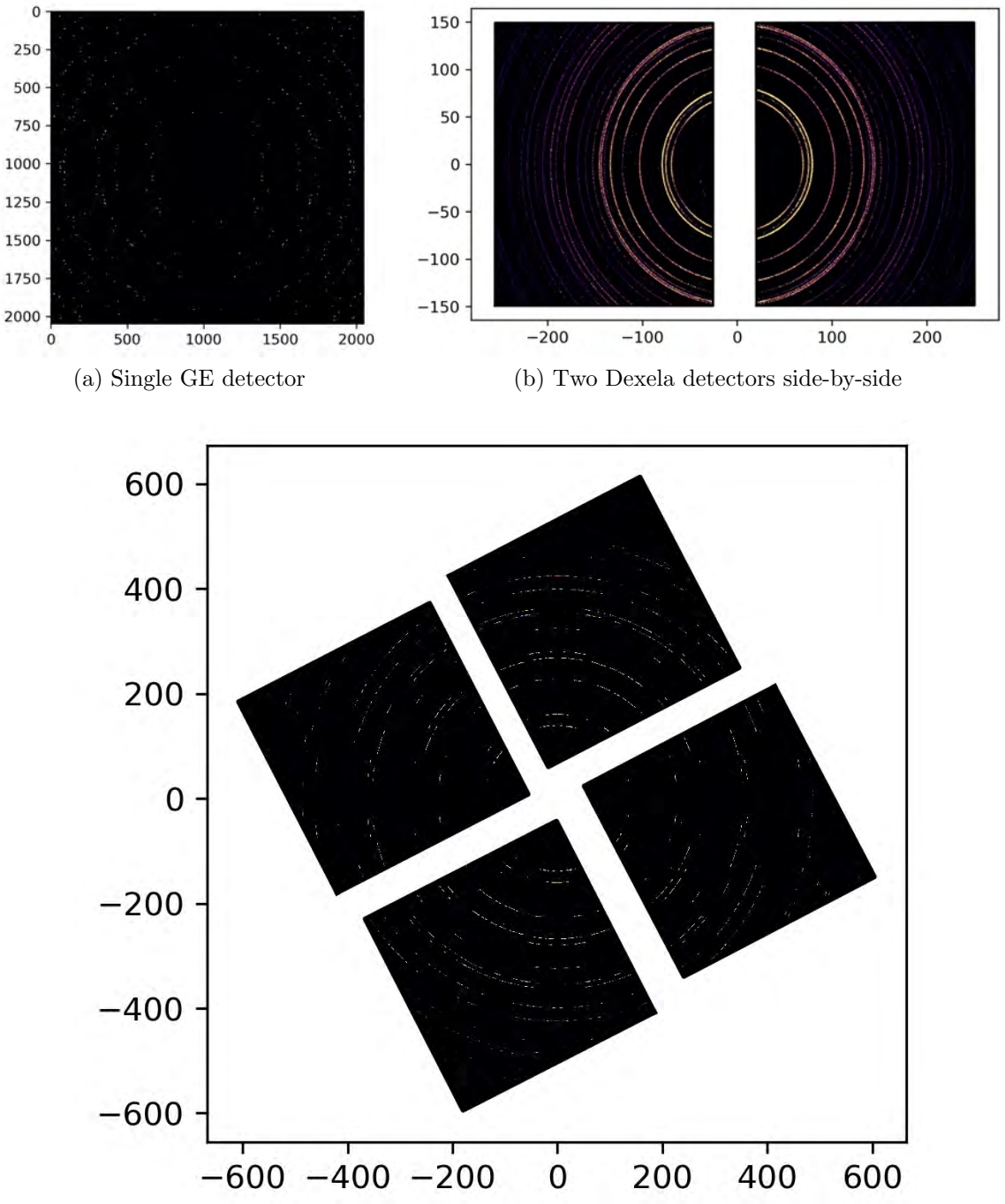

(a) Single GE detector

(b) Two Dexela detectors side-by-side

(c) Four GE detectors in "hydra" setup

Figure 1.4: There are currently three different detector setups being used between APS and CHESS that are being studied.

Cartesian coordinates, and these values are binned into the detector pixel array. This process is shown in Figure 1.5.

After trying this method, it was discovered that due to the 200 μm pixel size, there was limited COM resolution. For real data, the reduction algorithm uses the shape of the peak and interpolation to get sub-pixel resolution, but the initial algorithm is only simulating point-sharp diffraction. To take care of this, a Gaussian blur was added to mimic the point spread inherent in real x-ray measurements.

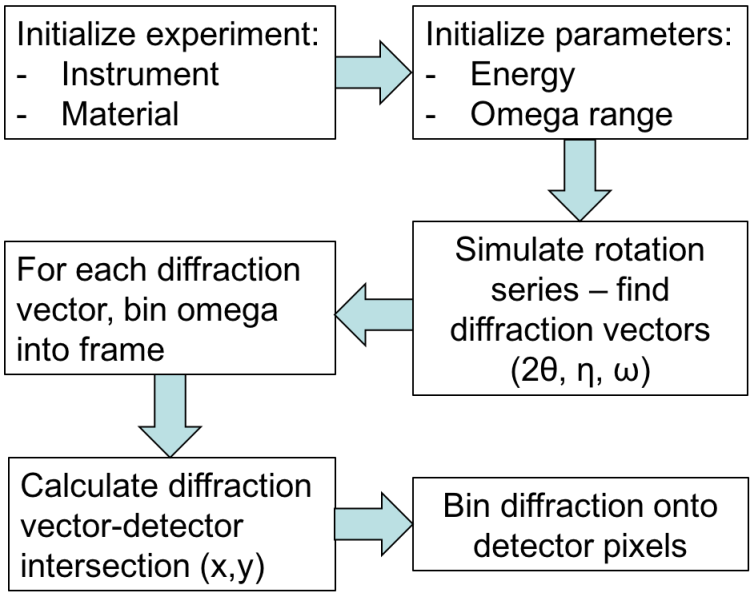

Figure 1.5: Flow chart explaining the initial design of the diffraction simulator.

First, a Gaussian blur filter was calculated on a 75×75 square (Fig. 1.6a). This can be binned into different sized patches to simulate different sized point spreads (Fig. 1.6b-d).

Now, the algorithm has an extra two steps to make the Gaussian blur filter then a grid is meshed around the calculated coordinates of the intersection between the diffraction vector and detector intersection and the filter is applied, and that is binned into the detector pixel array (Fig. 1.7).

1.3 Results

Simulations were run with a single orientation located on the rotation axis in the center of the x-ray beam, 100 μm away from the center in all three directions, and 500 μm away from the center in all three directions. The reduction of the data from the simulations show that the errors in COM increase the further away the grain is from the rotation center (Fig. 1.8). The error also increases with increasing patch size or point spread. Additionally, the error in the y direction is greater and increases more rapidly with increasing patch size, which can be attributed to the constraints of the experiment. The x and z directions are constrained by the omega rotation while the y direction is not.

A real dataset of a single crystal ruby rotated 360° with a 0.1° step size was taken at APS, and this was used to study the effects of different rotation step sizes. The ruby has little orientation gradient, thus the majority of the point spread present in the x-ray peaks (Fig. 1.3a) can be attributed to the instrument and detector broadening. The 0.1° frames were summed to create images representative of 0.2°, 0.3°, 0.4°, 0.5°, 1.0°, 2.0°, 3.0°, 4.0°, 5.0°, 6.0°, 8.0°, and 10.0° step size datasets. The 0.1° dataset was assumed to be the ground truth. It was found that the COM error and strain errors stayed approximately the same as the step size increased, but the orientation error increased (Fig. 1.9).

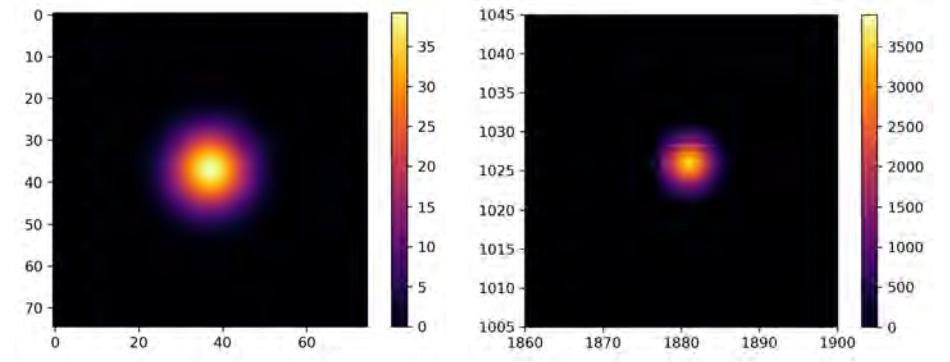

(a) Gaussian Filter

(b) 2.4 μm patch

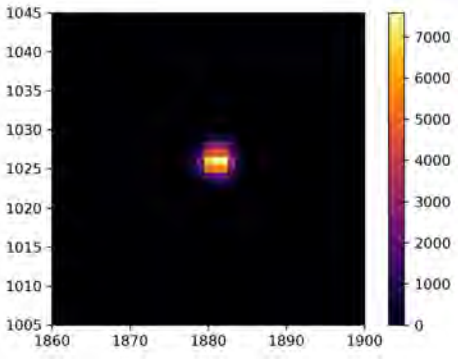

(c) 1.6 μm patch

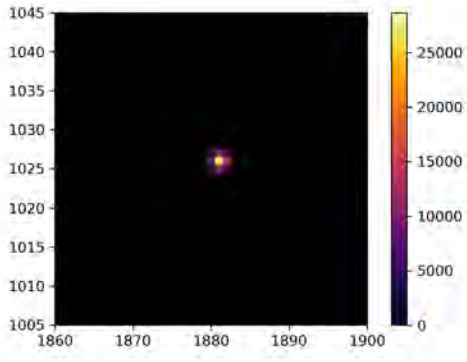

(d) 0.8 μm patch

Figure 1.6: A Gaussian filter was applied to each x-ray peak then binned into the detector pixels.

1.4 Discussion

Currently we are working with the detectors group at APS to get a more quantitative description of the detector point spread for both the GE and Dexela detectors. Additionally, there is a need for an intensity model which takes into account grain size, structure factor, detector effects, deformation, etc. There is currently an major effort being undertaken at LLNL to tackle this problem.

1.5 Future Work

Once the study on the bias error in the experimental setup is completed, a study will be done on the sensitivity of the ff-HEDM technique to material parameters such as crystal structure, grain size distribution in a polycrystal, number of grains, strain tensor, and centroid location.

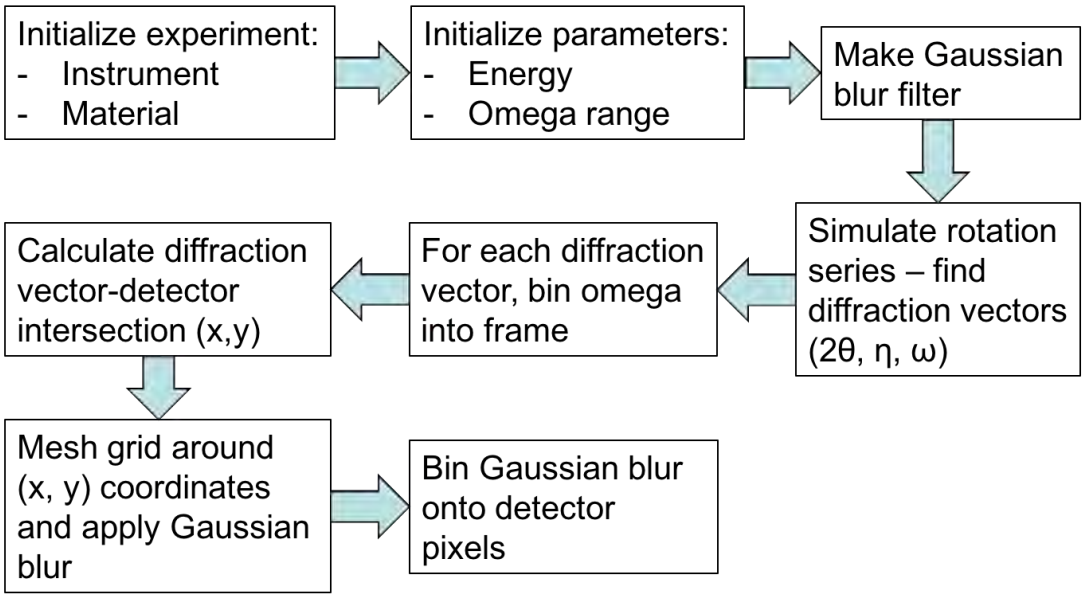

Figure 1.7: Flow chart explaining the current design of the diffraction simulator.

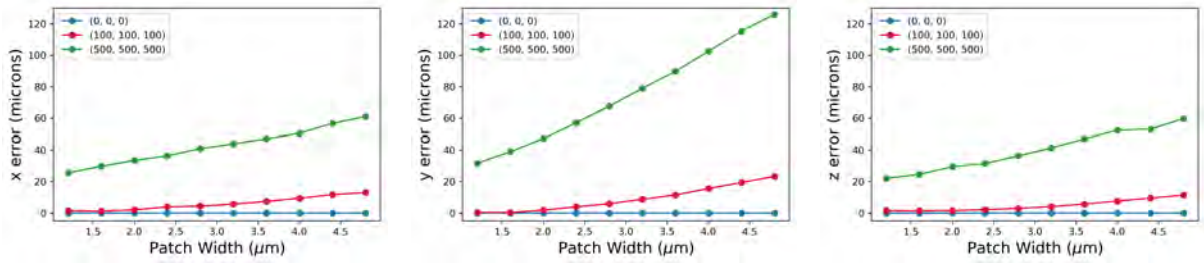

(a) (b) (c)

Figure 1.8: The COM errors increase as the grain moves further away from the rotation axis center. The errors also increase with increasing point spread.

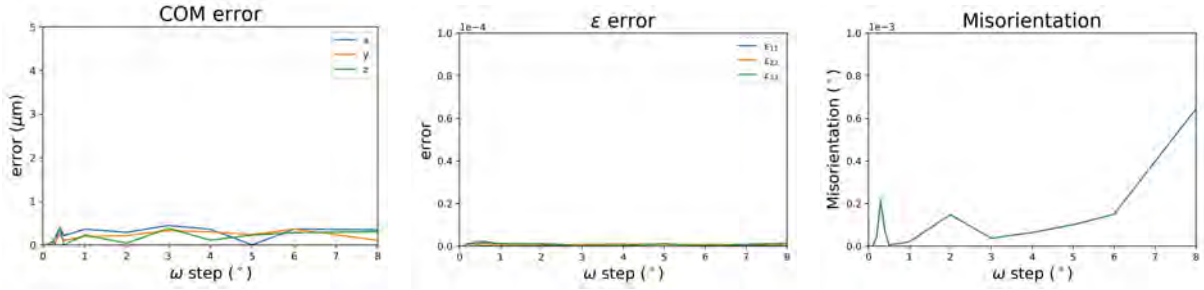

(a) (b) (c)

Figure 1.9: The 0.1° images from the ruby experiment were summed to create images representative of different rotation step sizes.

Representative Volume Element for Elasticity and Plasticity

Rachel E. Lim, Anthony D. Rollett

A representative volume element (RVE) is the smallest possible volume element of a material which is statistically representative of the macroscopic properties [5]. Due to the amount of time collecting and reducing HEDM data takes, one question of great importance to the community is: *What is the smallest possible volume we can scan to still get statistically significant data?* This section takes the experimental data from Pagan *et al.* and attempts to answer this question. It is being assumed in this work that the volume used in this experiment is greater than the RVE needed to study elastic and plastic behavior in this material.

2.1 Experiment Description

Pagan *et al.* [6] used statistics to draw conclusions on slip system strength (CRSS). 58 ff-HEDM scans were taken of a 1 mm tall volume of Ti-7Al as the sample was loaded to 2.5% strain (Fig. 2.1). A probability distribution function (PDF) is fit to the upper part of the RSS distributions for each slip system at each strain level (Fig. 2.2) which has the form,

$$f = A\left(1 - \tanh\left(\frac{2(\tau - \tau^*)}{w_\tau}\right)\right) \tag{2.1}$$

where A = a fitting constant, τ^* = the average slip system strength, and w_τ = the width of the distribution. The slip system strength was plotted as a function of macroscopic strain (Fig. 2.3, and it was found that the basal, prismatic, and pyramidal $\langle$a$\rangle$ slip systems softened after initial yield while the pyramidal $\langle$c+a$\rangle$ slip systems hardened rapidly, causing the macroscopic stress-strain curve to appear elastic-perfectly plastic.

2.2 Methods

Ten volume elements of different sizes were created from the full data set all the way down to a volume height of 0.2 mm. Due to the 20 μm resolution of the ff-HEDM technique, some of the centroids in the full data set lie just outside the $\pm$0.5 mm bounds. For each new dataset, the grains were filtered out by centroid location 10 μm at a time, resulting in fewer grains for smaller volumes as seen in Table 2.1.

Box Height (mm)	Full data	1	0.9	0.8	0.7	0.6	0.5	0.4	0.3	0.2
Number of Grains	361	334	275	241	197	168	139	106	65	33

Table 2.1: The number of grains in a box decreases as the height being used decreases.

For each data set, the RSS values were calculated for all the slip systems for each grain at each of the 58 data points. Then, a histogram for each slip system family was computed

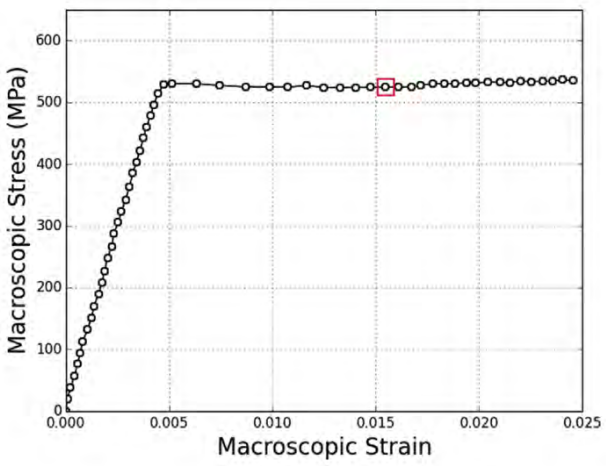

Figure 2.1: Macroscopic stress-strain curve for the experiment in Pagan *et al.* [6] with marks where each of the 58 ff-HEDM scans were taken.

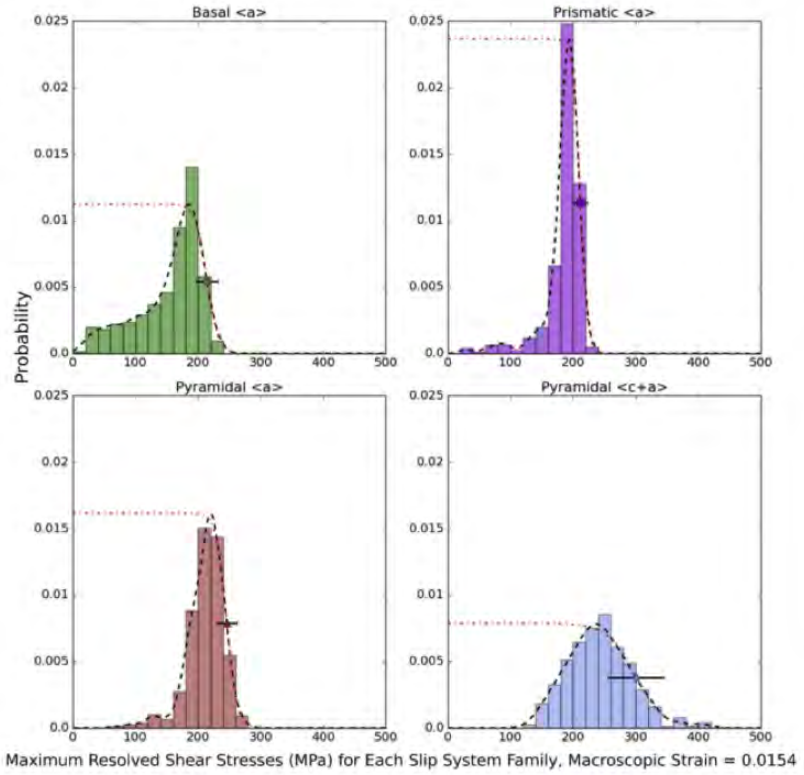

Figure 2.2: The RSS distributions with the appropriately fit PDF for each of the different slip systems at a macroscopic strain of 0.0154. Figure from Pagan *et al.* [6].

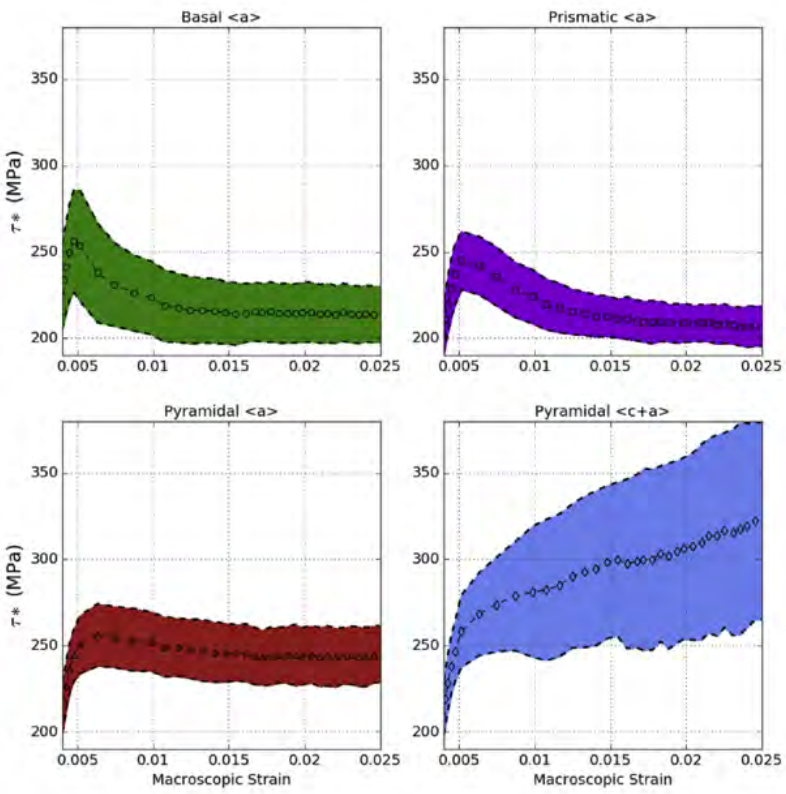

Figure 2.3: The slip system strength curves were plotted for each of the four major slip systems as a function of macroscopic strain. Figure from Pagan *et al.* [6].

at each of those same data points. The Hellinger distance was calculated between the original full dataset and each smaller dataset.

2.2.1 Hellinger Distance

Hellinger distance is a metric that is used to quantify the similarity between two probability distributions. For two discrete probability distributions, $P = (p_1, ..., p_k)$ and $Q = (q_1, ..., q_k)$, the Hellinger distance can be found to be

$$H(P, Q) = \frac{1}{\sqrt{2}} \sqrt{\sum_{i=1}^{k} (\sqrt{p_i} - \sqrt{q_i})^2} \tag{2.2}$$

The more similar two distributions are, the lower the Hellinger distance will be. Therefore, a large Hellinger distance would mean that the results are not converging, indicating the volume element being used is smaller than the RVE.

2.3 Results

The nominal yield for this experiment occurs just before 0.5% strain. For all of the slip systems, there is an increase in the Hellinger distance just before this point which matches with where some grains start slipping (Fig. 2.4).

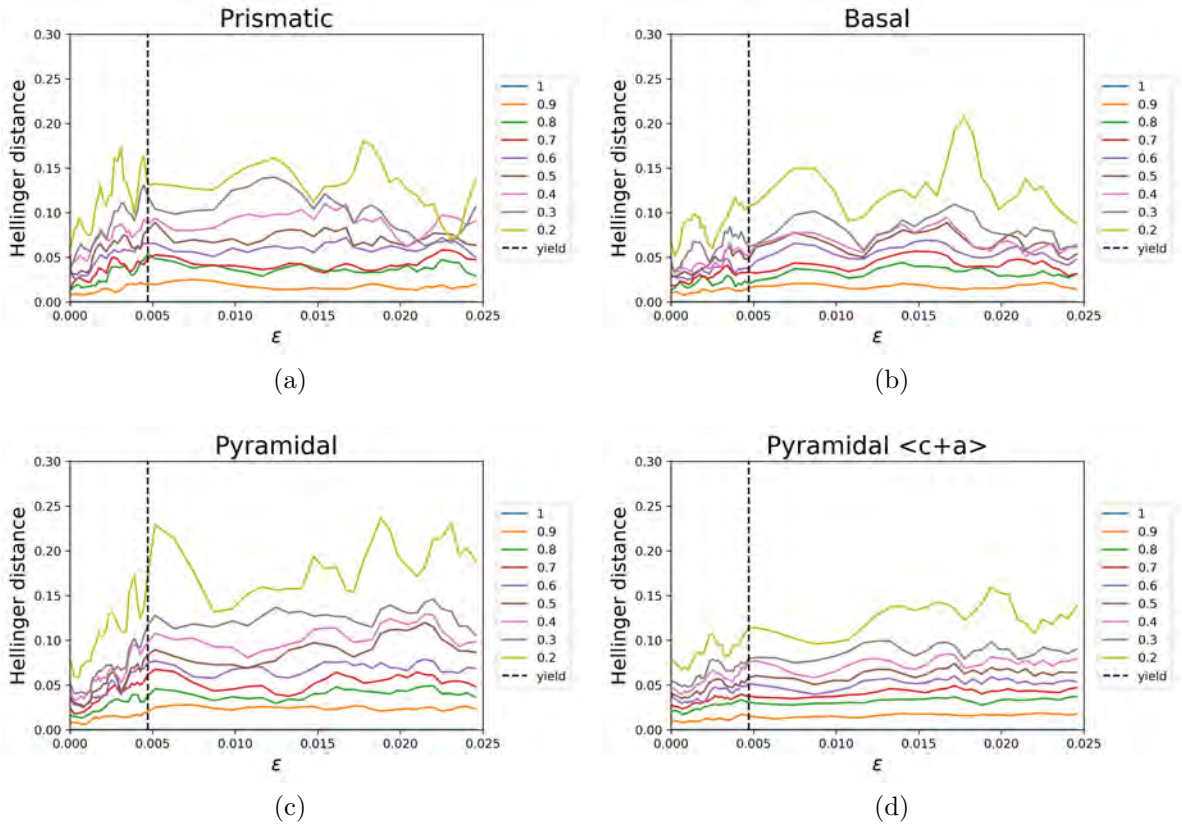

(a) (b)

(c) (d)

Figure 2.4: For all slip systems, there is a slight increase in Hellinger distance right before the marked nominal yield.

Additionally, as the size of the volume of material, and subsequently the number of grains, is decreased, the Hellinger distance increases indicating a distribution that is increasingly different from the original distribution (Fig. 2.5).

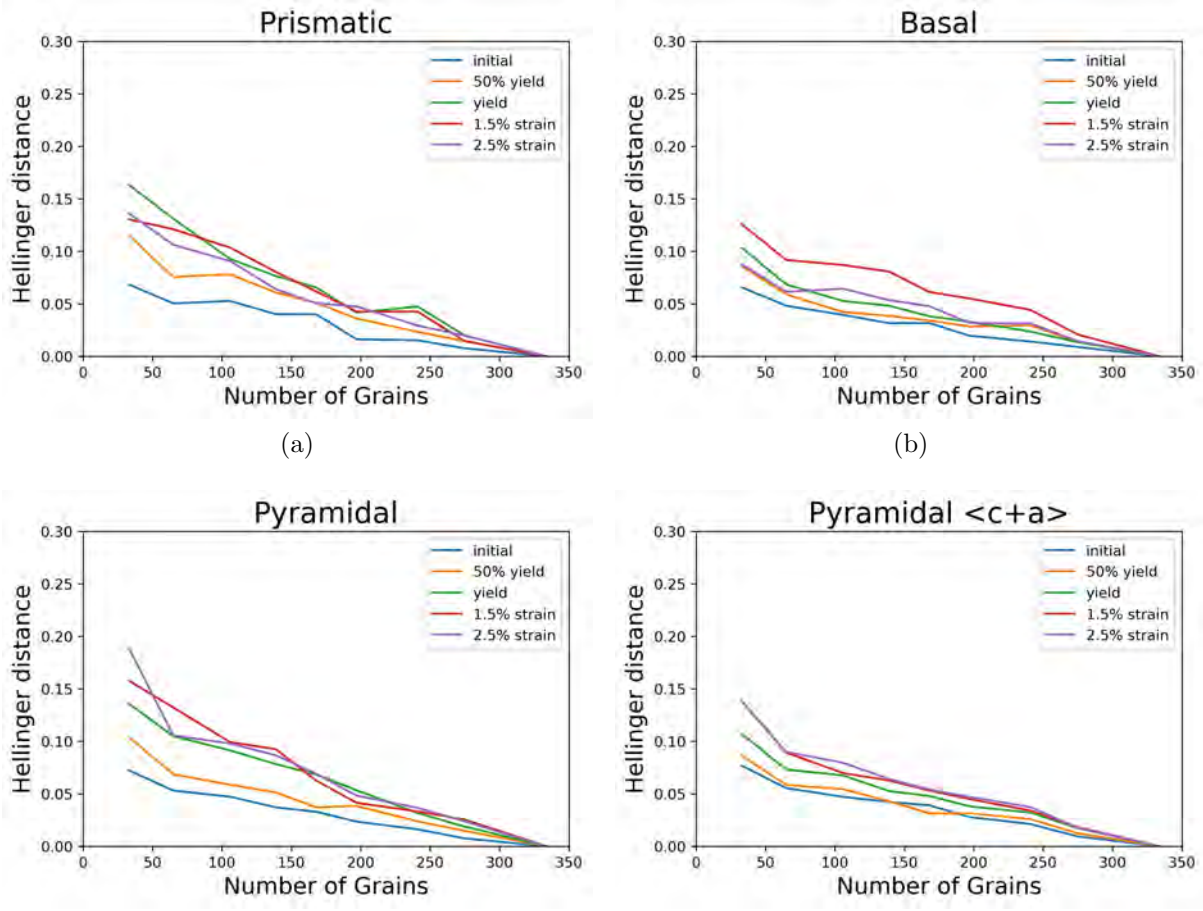

Figure 2.5: It is a consistent trend where the more grains being used in the data analysis, the more converged the answer gets for all of the slip systems at all of the different strain values.

Thermal Expansion of Ti-7Al

Rachel E. Lim, Darren C. Pagan, Donald E. Boyce, Anthony D. Rollett

3.1 Introduction

In hexagonal metals, anisotropic coefficients of thermal expansion (CTEs) are believed to generate the majority of type II residual stresses, i.e., microscale stresses which remain even after the removal of all external loads [7], during cooling from high-temperature processing conditions [8, 9]. These type II residual stresses affect the local variations in stress, and thus can play a critical role in either accelerating or suppressing the development of damage that leads to premature failure. Thus, the prediction of failure initiation hinges on residual stress instantiation that in turn relies on accurate CTE values (and their ratios). However, there is little agreement in the literature on the CTEs for these metals [10], and notably the reported CTEs for titanium (Table 3.1) vary from 9.26 $\times$ 10^{-6}/°C to 13.17 $\times$ 10^{-6}/°C, lacking agreement even on the ratio between α_a and α_c all of which motivated a more detailed examination of this phenomenon.

Year	**Paper**	α_a	α_c	α_v	**Temp. Range (°C)**
1942	Erfling [11]			8.24	20-40
1949	Greiner & Ellis [12]			9	30-200
1953	McHargue & Hammond [13]	11	8.8	10.3	25-225
1953	Berry & Raynor [14]	11.03	13.37	11.81	r.t.-700
1959	Spreadborough & Christian [15]	9.55	10.65	9.92	0-600
1962	Roberts [16]	10	9.95		
1962	Willens [17]	9.41	11.18		0-400
1968	Pawar & Deshpande [10]	9.5	5.6	8.2	28-155
1975	Touloukian [18]	9.23	9.57		
2019	Zheng et al.* [9]	**	***		r.t.-850

* Extracted from a simulation

** $5.23\times10^{-19}\,T^5 - 7.60\times10^{-16}\,T^4 + 3.84\times10^{-13}\,T^3 - 5.47\times10^{-11}\,T^2 + 8.39\times10^{-9}\,T + 1.91\times10^{-6}$

*** $7.76\times10^{-17}\,T^4 - 8.95\times10^{-14}\,T^3 + 5.46\times10^{-11}\,T^2 + 2.46\times10^{-10}\,T + 3.00\times10^{-6}$

Table 3.1: CTEs reported in literature (all CTE values except Zheng et al. are $\times$10^{-6}/°C).

Historically, thermal expansion of polycrystals has been studied using dilatometry [16, 19] where a rod-shaped specimen is placed in a furnace, and the change in length is measured as a function of temperature. However, this technique is not capable of probing the expansion along specific crystal directions, and only the effective macroscale thermal properties of the aggregate can be extracted. In order to study the anisotropic linear thermal expansion of a material, the characterization technique used must be capable of measuring expansion along different crystallographic directions. Powder diffraction [15, 10] is commonly employed to obtain the variation in lattice parameter(s), which is then used to calculate the CTEs, with the diffraction measurements providing information

on lattice plane spacings, from which lattice strains, due to both thermal and mechanical strains, can be calculated.

Anisotropic lattice expansion at the microscale becomes coupled to mechanical response as the material attempts to maintain local compatibility and stress equilibrium. Thermal expansion is equivalent to eigenstrain, i.e., stress-free strain, and for titanium and other hexagonal metals, the difference between the a-axis and c-axis expansion coupled with the variations in local crystallographic orientation results in the generation of elastic strains (and stresses) [20]. These mechanical strains are particularly difficult to decouple from thermal strains using powder diffraction methods. In this work, we utilize far-field high energy x-ray diffraction microscopy (ff-HEDM) measurements with *in situ* heating to extract the strain tensor for individual crystals within a polycrystalline aggregate as a function of temperature.

The ff-HEDM technique measures total lattice strain and cannot distinguish between the thermal and mechanical contributions, although the ability to measure full lattice strain tensors allows some decoupling of thermal and mechanical strains to be performed. We assume that non-zero shear strains and dispersion observed in normal strain components between grains is most directly the result of the development of mechanical strains, while the average strain across the ensemble of grains is the thermal strain. It should be noted that these variations in strains between individual grains due o neighborhood constraints cannot be isolated with powder diffraction, but is a direct result from ff-HEDM. This in turn allows for better understanding of the micromechanical interactions and subsequent interpretation of CTE measurements in a polycrystal.

The Ti-7Al studied in this work is a hexagonal close packed α-Ti alloy, and is similar to the α-phase in Ti-6Al-4V which is a commonly used alloy in the aerospace and biomedical industries. Ti-7Al is thermally anisotropic, making it interesting for thermal expansion and residual stress studies [15, 10, 21], and a significant amount of work has been done on characterizing the deformation of Ti-7Al using HEDM [22, 23, 24, 25, 6, 26].

Aging of Ti-7Al leads to short-range ordering (SRO) and the subsequent development of coherent α_2 Ti_3Al nanoprecipitates, which affects the mechanical behavior of titanium alloys with greater than 5% aluminum [27, 28]. The α_2 precipitates suppress twinning and increase slip on the basal planes [29, 30] and strengthen the material until the precipitates are sheared through dislocation slip [6].

3.2 Methods

Far-field high energy x-ray diffraction microscopy is a non-destructive, *in situ*, materials characterization technique, which can be used to track three-dimensional micromechanical evolution as a response to external stimuli. During the use of this technique, a sample is rotated about a single axis by an angle ω as the volume of interest is illuminated by the x-ray beam. When a family of planes $\{hkl\}$ in a grain satisfies the diffraction condition, it will diffract, producing a peak in intensity on the detector. Diffractograms are acquired at regular intervals integrated over $\Delta\omega$ no greater than 1.0°. Data collection over a full 360° rotation range allows observation of ∼50 to 100 diffraction peaks for each grain. In ff-HEDM measurements, the detector is placed ∼1 m away from the sample. In this setup, the diffraction peaks line up along Debye-Scherrer rings, with the small deviations of peak locations from idealized positions enabling ff-HEDM to determine the grain-averaged orientation, center of mass (COM), and lattice strain tensor of the grains

in the illuminated region of the sample [31, 32, 33].

In addition to the anisotropy of the CTEs for titanium, it has been shown that there is a possible temperature dependence [18, 21, 9]. The dependence of lattice parameter on temperature can be represented by $l(T)$. For a material, the CTE, α, for a given lattice parameter can be defined as

$$\alpha_l = \frac{\varepsilon_l}{dT} = \frac{\frac{dl}{l}}{dT} = \frac{1}{l}\frac{dl}{dT} \tag{3.1}$$

thus the temperature dependent CTE is

$$\alpha_l(T) = \frac{1}{l(T)}\frac{dl(T)}{dT} \tag{3.2}$$

3.3 Experiment

3.3.1 Material

The Ti-7Al material (nominal composition Ti-7.02Al-0.11O-0.015Fe wt.%) used for this work was cast as an ingot and hot isostatic pressed (HIP) to reduce porosity. It was extruded and then annealed at 962 °C for 24 hours before air cooling [34]. The aging of the Ti-7Al leads to short-range ordering (SRO) and the development of coherent α_2 Ti_3Al nanoprecipitates [28]. The samples were cut using electrical discharge machining to minimize the introduction of additional residual stresses. Figures 3.1b and 3.1c show reconstructions of the measured volumes from the two samples based on a Voronoi tessellation from the grain centers (as given by the ff-HEDM). The microstructures are equiaxed and have an approximate grain size of 50-100 μm with the textures of the samples were similar but not exactly the same.

3.3.2 Experiment description

Two thermal expansion experiments were performed on samples of Ti-7Al using the RAMS2 load frame [35] at the F2 beamline at the Cornell High Energy Synchrotron Source (CHESS). Fig. 3.1a shows a schematic of the experimental geometry. Each sample had a gauge length of 8 mm and a 1 mm x 1 mm cross-sectional area. The sample was heated to 850 °C at a rate of ∼8.5 °C/min using an x-ray transparent halogen bulb furnace with an elliptical mirror to focus the light onto the sample. The furnace was mounted onto the RAMS2 load frame as shown in Fig. 1 of Pagan et al. [26]. Far-field HEDM scans were acquired at regular intervals during heating, each with a full rotation of 360° and an ω interval of 0.25°, using a 61.3 keV x-ray beam. A 1.1 mm tall volume (with 50 μm on the top and bottom to allow for slit scattering) of ff-HEDM data was collected using two Dexela 2923 detectors (3888 x 3072 pixels, 74.8 μm pixel size) mounted side-by-side (Fig. 3.1a).

3.3.3 Data processing

The diffraction data was reduced using the HEXRD software package (`https://github.com/joelvbernier/hexrd`) [31]. The initial detector parameters were calibrated using powder patterns from a CeO_2 sample, and the grains in the Ti-7Al sample were

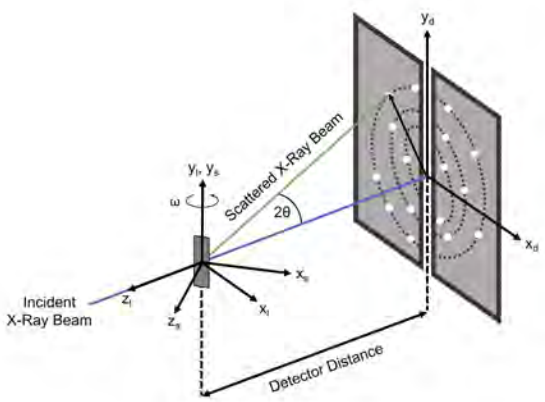

(a)

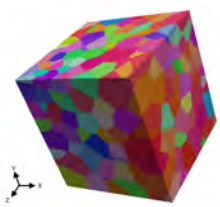

(b) Sample 1

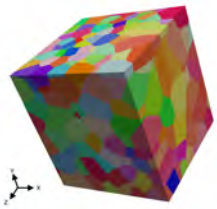

(c) Sample 2

Figure 3.1: (a) Schematic of the ff-HEDM experimental setup with two Dexela detectors side by side. The detector, laboratory, and sample frames are labeled as d, l, and s respectively, and the incident x-ray beam travels in the -z_d direction. (b)-(c) Three-dimensional renderings of the sample volumes grown from the centroids measured in the ff-HEDM

indexed and fit using lattice parameters of $a = 2.932$ Å and $c = 4.684$ Å. Then, the detector calibration was refined using a high completeness grain close to the vertical center of the scanned volume. The reduced grain data was filtered (completeness $> 90\%$ and normalized sum of square residuals $< 2 \times 10^{-3}$ [36]) so that only high fidelity grains remained.

3.4 Results

3.4.1 Ti-7Al coefficients of thermal expansion

Figure 3.2 shows the lattice parameters as a function of temperature. The white squares represent the average value for the ensemble of grains at a given temperature while the colored bands span the 10^{th} through 90^{th} percentile of the spread. The lattice parameters for each grain were calculated at each temperature by applying the stretch tensor (simply the identity tensor added to the lattice strain tensor for small strains) to the symmetrically equivalent basis vectors (in order to account for crystal symmetry) and taking the magnitude of the deformed lattice vectors. Then, the average lattice parameter for the entire ensemble of grains is used as the lattice parameter of the material at that temperature. As expected, the a-parameter and c-parameter expand monotonically with increasing temperature. To confirm that reasonable results were being obtained,

the ff-HEDM data was reduced to 2θ scans by summing over images in ω to create a representative powder pattern, and the lattice parameters were extracted. The lattice parameters calculated using this method, and those from the aforementioned ff-HEDM method were in good agreement (see Appendix **??**).

The temperature dependent directional CTEs are shown for both samples in Figs. 3.3a and 3.3b respectively, where the bars represent the error bounds calculated from a Monte Carlo calculation, while Fig. 3.3c shows the the relative CTE ratio, α_c over α_a. This value increases with respect to temperature. The CTEs were calculated according to Eq. 3.2, and the ratios of α_a and α_c were then calculated from this data. Although the directional CTEs exhibited minor variations, in general, both follow similar trends with a peak near 600 °C. Further research is required to understand the origin of these maxima. The ratio of α_c to α_a increased monotonically with heating, with a crossover in ratio from less than one to greater than one occurring at ∼170 °C as shown in Figure 3.3c. Additionally, the spread in lattice parameters broadens slightly with increasing temperature.

3.4.2 Ti-7Al grain strain and stress evolution

The distribution of σ_{VM} was plotted in figure 3.4 for each temperature in the thermal cycle. The σ_{VM} decreases until ∼700 °C when the spread of the distributions start to increase. As the samples cool, the mean and spread of the distribution of σ_{VM} decreases until the sample reaches ∼700 °C when they start to increase again until room temperature where both the final mean and spread of the distributions are less than the initial values.

Motivated by the possibility that certain grains may have experienced micro-plastic flow, the measured strains were used to calculate the elastic strain and subsequently the

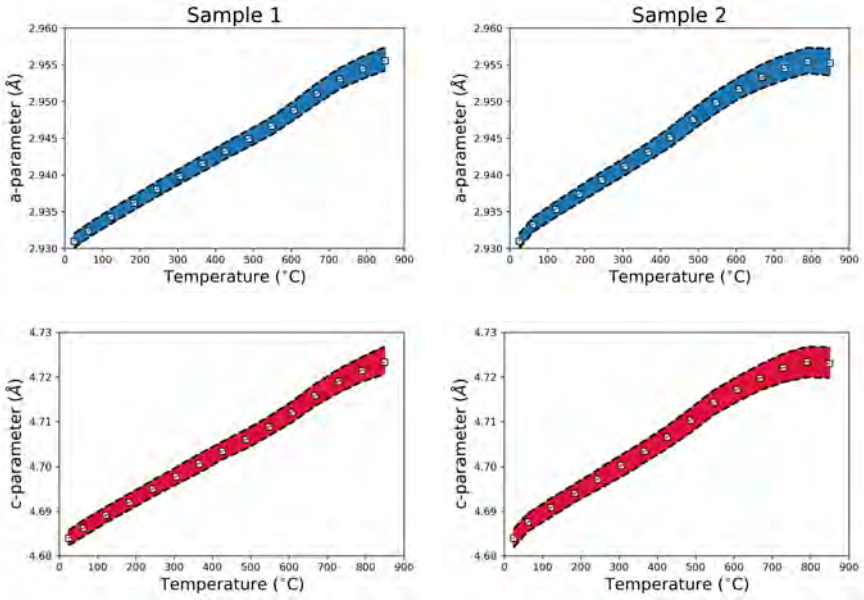

Figure 3.2: The (a)-(b) a-parameter and (c)-(d) c-parameter are plotted as a function of temperature for both samples, where the square glyphs represent the mean values, and the colored bands represent the 10th and 90th percentile. The a- and c-parameters expanded with respect to temperature as expected.

stress in each grain via temperature-dependent moduli from Fisher *et al.* [37]. The RSS values for all four slip systems were calculated by projecting the stress onto each individual system. Figure 3.5 shows values for the RSS on all of the slip systems decrease as a function of temperature. However, the mean values for the pyramidal ⟨c+a⟩ systems decrease until ∼700 °C when they start to increase slightly, similar to the σ_{VM} distributions. Additionally, the distributions for the prismatic ⟨a⟩ and the pyramidal ⟨a⟩ systems are tighter than the distributions for the basal ⟨a⟩ and the pyramidal ⟨c+a⟩ systems.

3.5 Discussion

3.5.1 Comparison of CTEs with literature

As mentioned, the CTEs for titanium reported in literature (Table 3.1) vary from a low of 5.6 × 10^{-6}/°C to a high of 13.6 × 10^{-6}/°C and show little agreement even for the ratio of α_a to α_c. Based on the results of this study (Fig. 3.3), the temperature dependence of the CTEs may explain the observed spread of values and ratios. Most reported values in the literature do not take temperature dependence into account, whereas we find that the CTE ratio is less than one at low temperatures and greater than one at high temperatures,

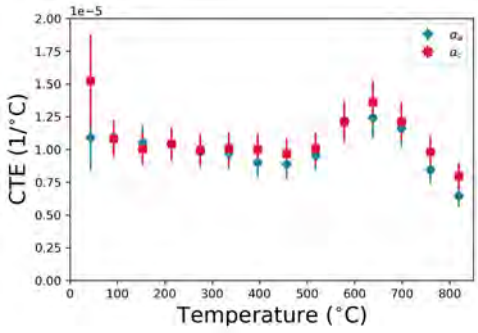

(a) Sample 1

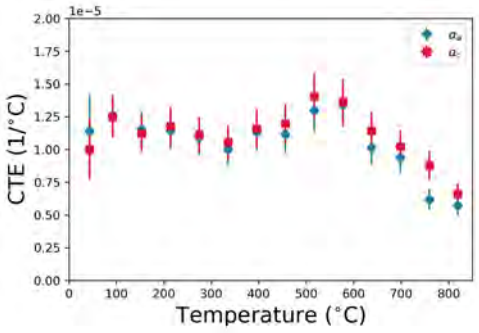

(b) Sample 2

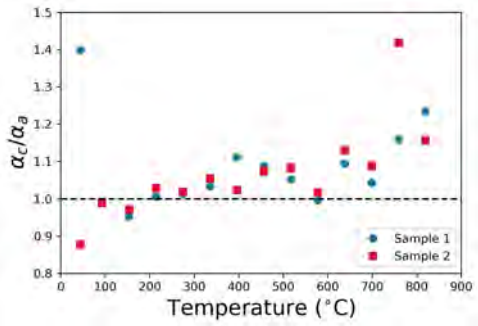

(c)

Figure 3.3: (a)-(b) Both α_a and α_c decrease, then increase, then decrease again with as the samples are heated. Error bounds are given from a Monte Carlo calculation. (c) The ratio of α_c to α_a increases as a function of T. The ratio is less than one at low temperature and is greater than one at high temperature. This variation helps to explain some of the inconsistency in the ratios reported in the literature. The CTEs are anisotropic (with $\alpha_c < \alpha_a$) at RT, reasonably isotropic from 150 to 600 °C, and anisotropic (with $\alpha_c > \alpha_a$) above this.

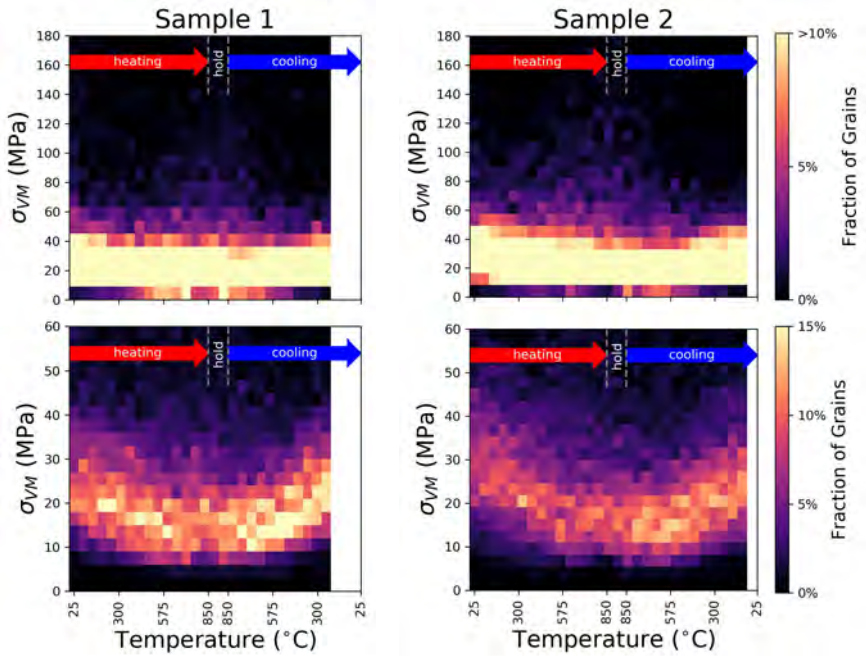

Figure 3.4: The distribution of von Mises stress is plotted at each temperature. The larger range (top) shows an increase at the high end of the distribution at high temperature. The smaller range (bottom) shows that the von Mises stresses are lower after the thermal cycle, and the distributions become tighter. The white space on the right is where the x-ray beam was lost before the experiment reached room temperature.

therefore the temperature range in which the CTEs are measured is critical.

For example, McHargue and Hammond [13] and Pawar and Deshpande [10] measured the CTEs up to 225 °C and 155 °C respectively, and report values where $\alpha_c < \alpha_a$. This is within the temperature range where the present work shows that the α_c to α_a ratio is less than one. By contrast, Berry and Raynor [14] and Spreadborough and Christian [15] measured the CTE up to 700 °C and 600 °C, and report values where $\alpha_c > \alpha_a$. In this temperature range, the present work confirms that the ratio of α_c to α_a is greater than one. This also concurs with the results from Zheng et al. [9], who showed a crossover point around 690 °C. However, these measurements were made in commercial purity titanium and were were extracted from a simulation, and the experimental CTEs were not shown. The crossover point found here at 170 °C for the Ti-7Al alloy is lower than what was found in commercial purity Ti [9] but follows the same trend.

In addition, the CTE values for the two axes vary systematically with temperature, with three distinct sections in the curve (Fig. 3.3a-b). The first section is the decreasing CTE of the Ti-7Al material with both the α and α_2 phases present, the second region is the increasing CTE where the α_2 nanoprecipitates are dissolving into the material, and the third region is the Ti-7Al material with only the α phase. It is expected that if the material was to be heated with a more gradual ramp rate, the increase in CTE would be more sharper and more distinct as the α_2 should all dissolve at a single temperature.

It is important to note that with 7 wt% Al (12 at%) , the Ti-7Al material falls within the two-phase region of the Ti-Al phase diagram. However, the boundary between the α and $\alpha + \alpha_2$ regions is not well defined as can be seen in figure 3.6. The

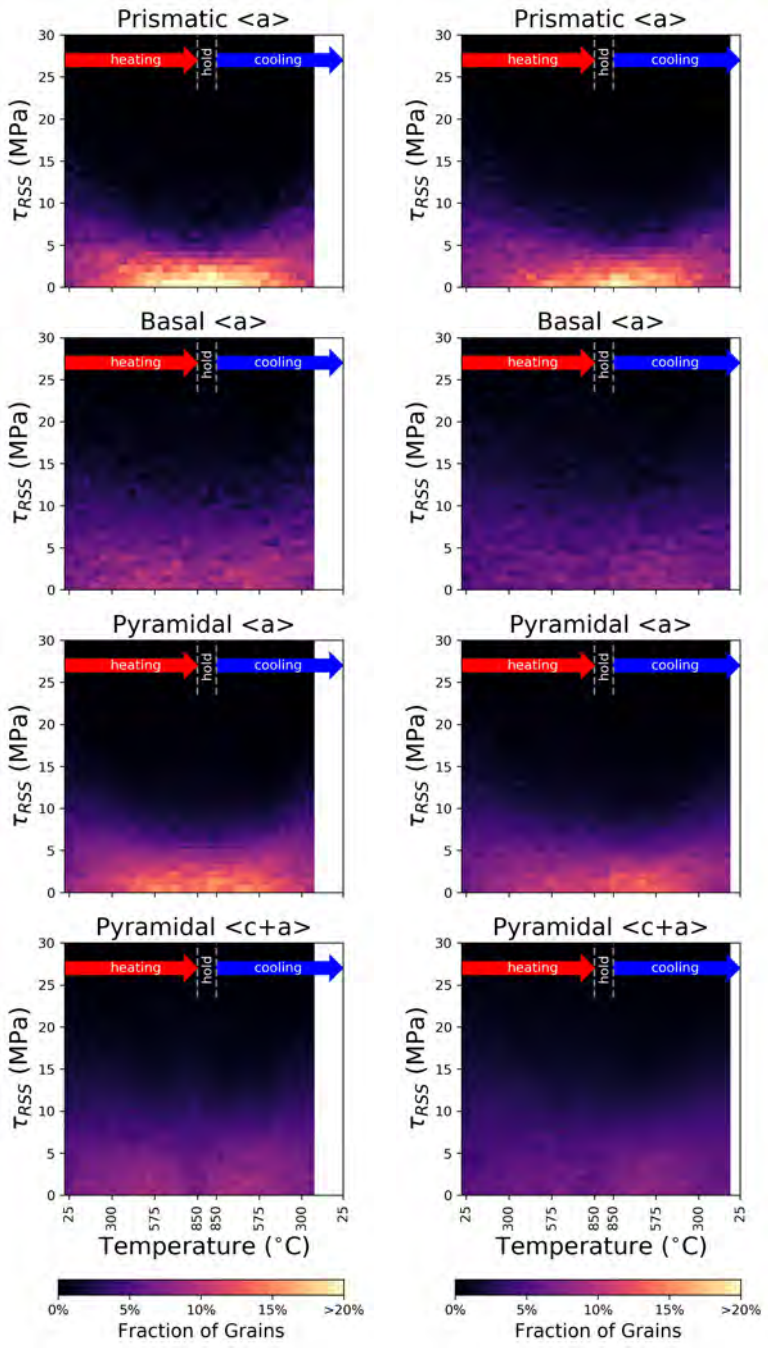

(a) Sample 1 (b) Sample 2

Figure 3.5: The resolved shear stresses (RSS) for the prismatic ⟨a⟩, basal ⟨a⟩, pyramidal ⟨a⟩, and pyramidal ⟨c+a⟩, were calculated for (a) sample 1 and (b) sample 2 as function of temperature from the measured strain tensor and temperature dependent single crystal elastic modulus. The RSS values drop with temperature until ∼700 °C when upper tail of the distributions for the pyramidal ⟨c+a⟩ RSS values starts to increase. The white space on the right is where the x-ray beam was lost before the experiment reached room temperature.

3.5.2 Micromechanical Response

At 700 °C, the RSS values for the basal, prismatic, and pyramidal ⟨a⟩ slip system families continue to decrease whereas the pyramidal ⟨c+a⟩ slip systems increase markedly.

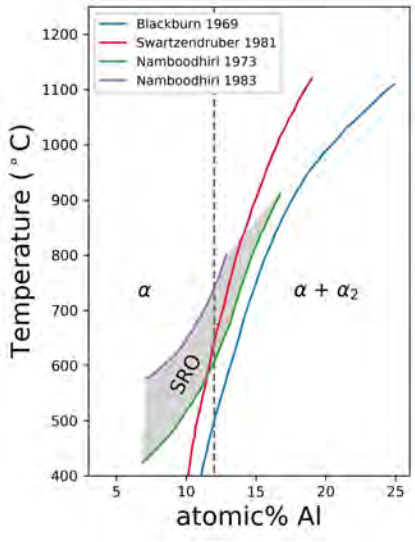

Figure 3.6: Ti-rich section of the Ti-Al phase diagram adapted from [38, 39, 40, 41] where 12 at% Al is equal to 7 wt%.

The pyramidal ⟨c+a⟩ slip system is harder than the other three [42, 26], so by 700 °C, the other three are soft enough that they experience slip causes new grain interactions and a stress build up on the pyramidal ⟨c+a⟩ systems which still have some strength.

This build up of stress on the pyramidal ⟨c+a⟩ slip systems is enough that it causes an increase in upper tail of the σ_{VM} distribution at high temperature. As the material is cooled back down to room temperature, the grains contract, and the internal stresses follow the reverse path as the heating.

However, what is relevant here is whether the RSS values exceed their associated CRSS. Williams *et al.* [42] measured CRSS values for Ti-6.6Al the prismatic and basal slip systems in compression, The values for Ti-7Al determined by Pagan *et al.* [26] at room temperature and at 355 °C follow the trend line fit to the Ti-6.6Al data that shows an exponential decay in the slip system strength as a function of temperature. Figure 3.7 shows the measured CRSS values along with the exponential fit as well as a boxplot for RSS values at the highest temperature. In the case of the prismatic slip system, the RSS values do not significantly exceed the CRSS but, for the basal system, there are many grains in the upper tail whose basal RSS exceeds the CRSS.

3.6 Conclusion

In summary, ff-HEDM has been used to calculate the temperature dependent CTEs for hexagonal Ti-7Al with the primary finding that the ratio of α_c to α_a changes from less than one to greater than one, resolving the discrepancies found for Ti thermal expansion data found in the literature. CTE maxima were found between 500 and 650 °C, and ff-HEDM allowed calculation of confidence bounds for the CTEs. Note that using incorrect CTE values and ratios can result in type II residual stress predictions that are opposite of what would occur (i.e., tension to compression and vice versa). In the future, the temperature dependent relationship of the CTEs for hexagonal materials, particularly in titanium alloys, will vastly improve the accuracy of micromechanical modeling used to study fatigue properties. It is already clear that most "well annealed" samples contain

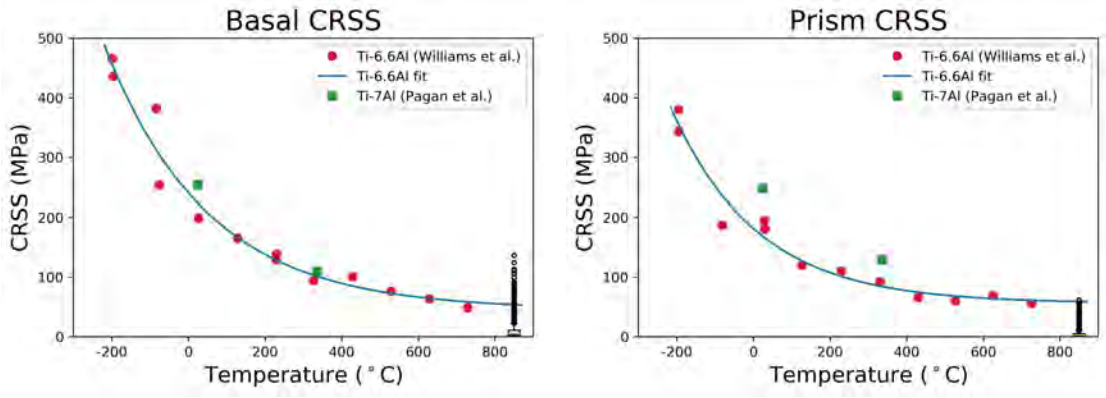

(a) (b)

Figure 3.7: (a) Plot of the basal CRSS as a function of temperature with a boxplot of the RSS values superimposed to show that the outlier RSS values easily exceed the CRSS at high temperature. (b) Plot of the prismatic CRSS as a function of temperature with a boxplot of the RSS values superimposed to show that even the outlier RSS values do not significantly exceed the CRSS at high temperature. CRSS values taken from Williams *et al.* [42] and Pagan *et al.* [6, 26]

.

type II residual strains [32], and instantiating micromechanical simulations with these strains is essential for accurate results [36].

3.7 Supplementary Material

3.7.1 Calculating the Lattice Parameters

Letting $\mathbf{X}$ be the undeformed, reference state and $\mathbf{x}$ be the deformed state of interest, the deformation gradient tensor $\mathbf{F}$ is defined as

$$\mathbf{F} = \frac{d\mathbf{x}}{d\mathbf{X}} \tag{3.3}$$

The polar decomposition of $\mathbf{F}$ gives

$$\mathbf{F} = \mathbf{VR} = \mathbf{RU} \tag{3.4}$$

where $\mathbf{V}$ is the left stretch tensor, $\mathbf{U}$ is the right stretch tensor, and $\mathbf{R}$ is the rotation matrix. $\mathbf{R}$ is defined as the rotation matrix which takes a vector from the crystal frame to the sample frame which means that $\mathbf{V}$ stretches a vector in the sample frame and $\mathbf{U}$ stretches a vector in the crystal frame (Fig. 3.8).

The reduced ff-HEDM data gives both $\mathbf{V}^{-1}$ and the orientation. In order to find the average lattice parameters for each grain, the magnitude of all the equivalent lattice vectors are averaged. The crystal symmetry must be taken into account, which means that $\mathbf{V}$ has to be converted into $\mathbf{U}$ using

$$\mathbf{U} = \mathbf{RVR^T} \tag{3.5}$$

so that the stretch can be applied to each symmetrically equivalent lattice vector. $\mathbf{U}$ and $\mathbf{R}$ can be applied to the undeformed lattice basis vectors of a crystal to find the deformed

vectors.

$$[\mathbf{a}', \mathbf{b}', \mathbf{c}'] = \mathbf{U}(\mathbf{R}[\mathbf{a}, \mathbf{b}, \mathbf{c}]) \tag{3.6}$$

Since Ti-7Al is a hexagonal material, $\mathbf{O}_{622}$ can be used to represent the symmetry operators. If $\{\mathbf{h}\}$ represents the $[\mathbf{a}', \mathbf{b}', \mathbf{c}']$ calculated from equation 3.6, then

$$\{\mathbf{h}'\} = \mathbf{O}_{622}\{\mathbf{h}\} \tag{3.7}$$

where $\{\mathbf{h}'\}$ is the set of all symmetrically equivalent deformed lattice vectors, the average of the magnitudes of which are the lattice parameters.

3.7.2 Powder Diffraction Comparison

The ff-HEDM images were summed over the ω range to create a representative powder pattern. This was treated as a typical powder diffraction pattern, and the lattice parameters were extracted. The lattice parameters calculated using this method, and those from the aforementioned ff-HEDM method were in good agreement

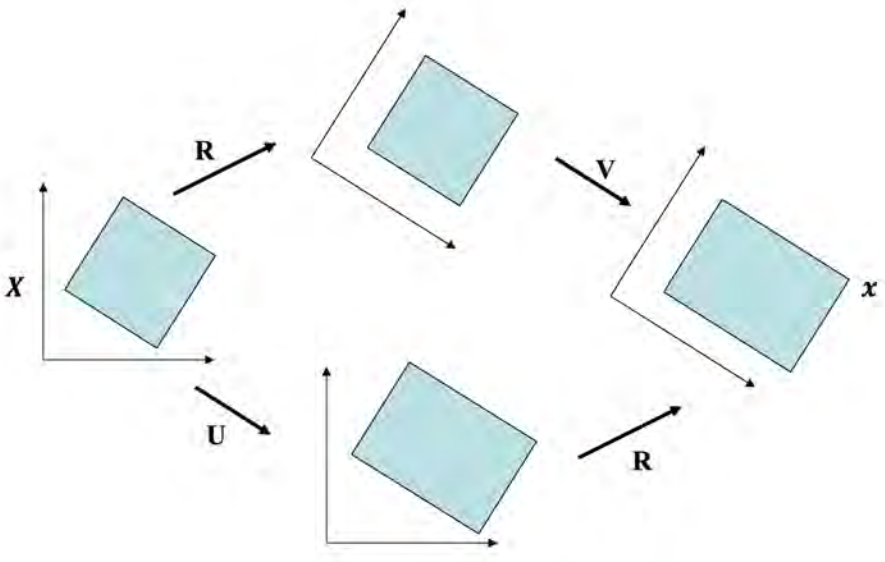

Figure 3.8: Given an undeformed state, $\mathbf{X}$, and a deformed state, $\mathbf{x}$, the deformation gradient tensor is defined as $\mathbf{F} = \frac{d\mathbf{x}}{d\mathbf{X}}$. The polar decomposition of $\mathbf{F}$ gives $\mathbf{F} = \mathbf{VR} = \mathbf{RU}$, where $\mathbf{U}$ stretches vectors in the crystal frame, $\mathbf{V}$ stretches vectors in the sample frame, and $\mathbf{R}$ takes the sample frame and rotates it to the crystal frame.

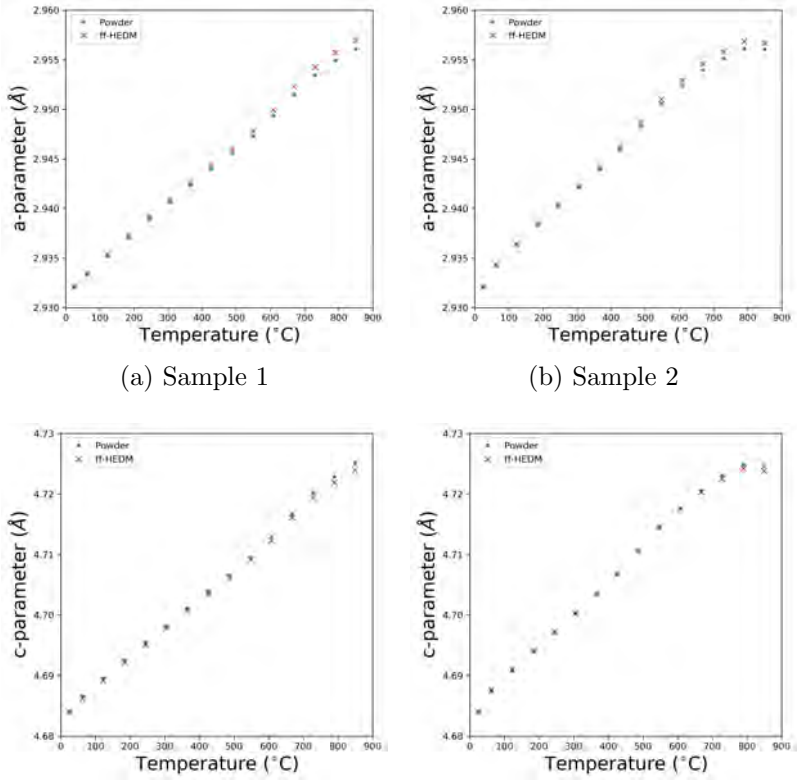

(a) Sample 1 (b) Sample 2

(c) Sample 1 (d) Sample 2

Figure 3.9: The ff-HEDM images were integrated across the entire rotation series, and the integrated images were treated as powder diffraction patterns. The calculated lattice parameter matched those calculated from the ff-HEDM method.

Micromechanical Evolution of Ti-7Al Under Cyclic Loading

Rachel E. Lim, Darren C. Pagan, Vahid Tari, Yu-Feng Shen,
Robert M. Suter, Anthony D. Rollett

4.1 Introduction

Fatigue is one of the major forms of failure in mechanical parts, yet we lack a significant understanding of what occurs on the mesoscopic (grain) level. Developments in materials characterization using high energy x-rays (>50 keV) at synchrotron light sources allow us to examine microstructure in three dimensions, giving us the ability to study microstructural evolution in a much deeper manner. In this work, a high energy x-ray diffraction microscopy experiment was conducted to map micromechanical strain evolution in a sample of Ti-7Al under the first 200 cycles of uniaxial tensile loading. It was expected that the sample would exhibit elastic shakedown, the process in which the plastic strains in a structure stabilize after a finite number of loading cycles [43, 44, 45].

4.1.1 High Energy X-ray Diffraction Microscopy

High energy x-ray diffraction microscopy (HEDM) is a non-destructive, *in situ*, materials characterization technique, which can be used to track three-dimensional microstructural evolution as a response to external stimuli. During the use of this technique, a sample is rotated through ω as the volume of interest is illuminated by the x-ray beam. When a family of planes, $\{hkl\}$, in a grain satisfies Bragg's law, it will diffract, producing a peak on the detector. Bragg's law is defined as:

$$\lambda = 2d_{hkl} \sin \theta_{hkl} \tag{4.1}$$

where λ is the x-ray wavelength, d_{hkl} is the lattice spacing of a family of planes, and θ_{hkl} is the diffraction angle.

The crystal lattice can be defined by its basis vectors $\mathbf{a}$, $\mathbf{b}$, and $\mathbf{c}$ where:

$$\|\mathbf{a}\| = a, \quad \|\mathbf{b}\| = b, \quad \|\mathbf{c}\| = c \tag{4.2}$$

$$\frac{\mathbf{b} \cdot \mathbf{c}}{bc} = \cos \alpha, \quad \frac{\mathbf{c} \cdot \mathbf{a}}{ca} = \cos \beta, \quad \frac{\mathbf{a} \cdot \mathbf{b}}{ab} = \cos \gamma \tag{4.3}$$

and $\{a,\ b,\ c,\ \alpha,\ \beta,\ \gamma\}$ represents the conventional parameterization of the crystal unit cell in the unloaded, reference temperature state (Fig. 4.1) where $\mathbf{a} \parallel \hat{\mathbf{X}}_c$ and $(\mathbf{a} \times \mathbf{b}) \parallel \hat{\mathbf{Z}}_c$. The transformation matrix that takes the lattice vectors, $\{\mathbf{a,\ b,\ c}\}$, into the right-hand orthonormal crystal frame, $\{\hat{\mathbf{X}}_c\ \hat{\mathbf{Y}}_c\ \hat{\mathbf{Z}}_c\}$, can be defined as:

$$\mathrm{A} = \begin{bmatrix} a & b\cos\gamma & c\cos\beta \\ 0 & b\sin\gamma & -c\sin\beta\cos\alpha^* \\ 0 & 0 & c\sin\beta\sin\alpha^* \end{bmatrix} \tag{4.4}$$

where $\cos\alpha^* = \frac{\cos\beta\cos\gamma - \cos\alpha}{\sin\beta\sin\gamma}$ [46]. The crystal orientation rotation matrix, α_{ij}, takes components from the crystal reference frame, $\{\hat{\mathbf{X}}_c\ \hat{\mathbf{Y}}_c\ \hat{\mathbf{Z}}_c\}$, to the sample reference frame, $\{\mathbf{X}_s\ \mathbf{Y}_s\ \mathbf{Z}_s\}$.

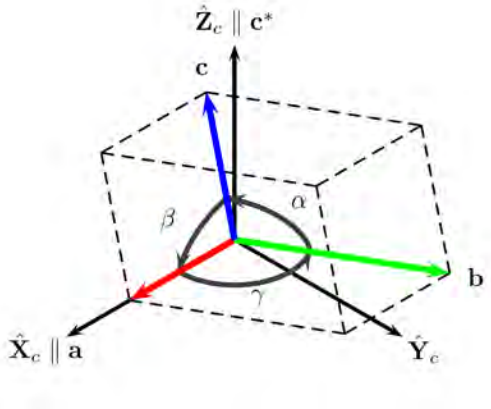

Figure 4.1: Convention for describing the crystal lattice using a triclinic primitive cell for geometric generalization where $\{\hat{\mathbf{X}}_c\ \hat{\mathbf{Y}}_c\ \hat{\mathbf{Z}}_c\}$ is in the crystal frame [47].

The reciprocal basis vectors, defined as:

$$\mathbf{a}^* = \frac{\mathbf{b}\times\mathbf{c}}{V}, \quad \mathbf{b}^* = \frac{\mathbf{c}\times\mathbf{a}}{V}, \quad \mathbf{c}^* = \frac{\mathbf{a}\times\mathbf{b}}{V} \tag{4.5}$$

where $V = \mathbf{a}\cdot\mathbf{b}\times\mathbf{c}$ is the volume of the primitive unit cell.

A reciprocal lattice vector, $\mathbf{G}_{hkl}$, can be used to describe a point in reciprocal space using the reciprocal basis vectors and the Miller indices for the lattice planes with normals parallel to $\mathbf{G}_{hkl}$ in reciprocal space:

$$\mathbf{G}_{hkl} = h\mathbf{a}^* + k\mathbf{b}^* + l\mathbf{c}^* \tag{4.6}$$

and geometrically means that:

$$\mathbf{d}_{hkl} = \frac{1}{\|\mathbf{G}_{hkl}\|} \tag{4.7}$$

A scattering vector, $\mathbf{Q}$, can be defined as:

$$\mathbf{Q} \equiv \frac{\mathbf{s}_o - \mathbf{s}_i}{\lambda} \tag{4.8}$$

where $\mathbf{s}_i$ is the unit vector representing the incident x-ray beam and $\mathbf{s}_o$ is the unit vector representing the diffracted x-ray beam. When the Bragg condition is fulfilled, $\mathbf{Q} = \mathbf{G}_{hkl}$ and diffraction occurs. As the sample rotates, $\mathbf{G}_{hkl}$ comes in and out of alignment with $\mathbf{Q}$, causing different grains to diffract at various ω values.

Far-field HEDM

In the case of far-field HEDM (ff-HEDM), the detector is placed ∼1 m away from the sample. In this setup, the diffraction peaks line up along Debye-Scherrer rings, allowing ff-HEDM to be used to find the orientations, center of mass (COM), and elastic strain state of the grains in the illuminated region of the sample [31, 32]. Each peak on the

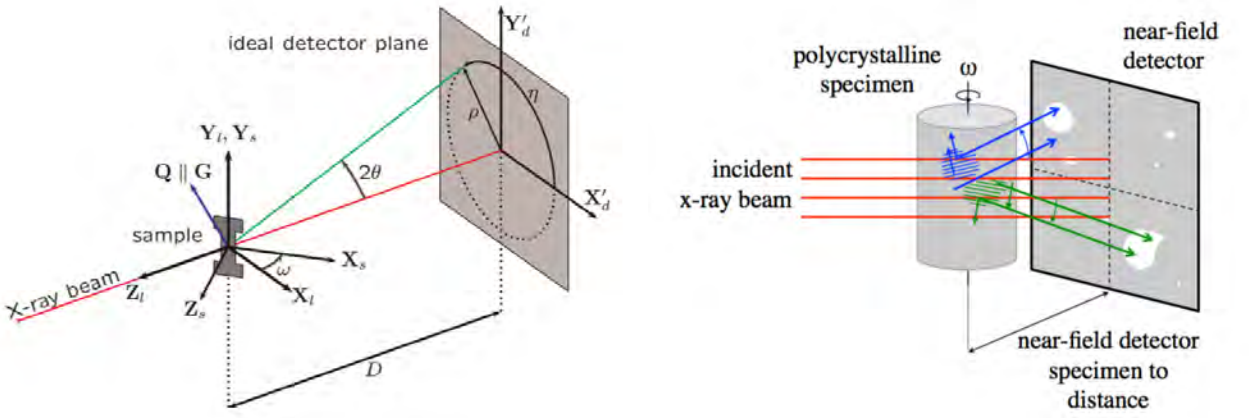

(a) (b)

Figure 4.2: Geometry of (a) ff-HEDM setup where $\{\mathbf{X}'_d\ \mathbf{Y}'_d\ \mathbf{Z}'_d\}$ is the detector frame, $\{\mathbf{X}_l\ \mathbf{Y}_l\ \mathbf{Z}_l\}$ is the laboratory frame, and $\{\mathbf{X}_s\ \mathbf{Y}_s\ \mathbf{Z}_s\}$ is the sample frame [31] and (b) nf-HEDM setup showing grain shapes on detector [48].

detector can be parameterized in terms of $(2\theta, \eta, \omega)$, where 2θ is the radial position, η is the azimuthal position, and ω is the average rotation angle position (Fig. 4.2a). In general, as a sample is deformed, deviations in 2θ are related to changes in d_{hkl}, which are associated with the elastic strain tensor, while deviations in η and ω are related to changes in orientation [49].

Reduction of ff-HEDM data is done in two steps: first, the sample is indexed to find orientation clusters, then the data is fit to optimize the orientation (3 parameters), COM (3 parameters), and elastic strain tensor (6 parameters). In order to index the sample, a set of orientations is generated from the diffraction data by back-projecting the measured data to define a set of crystallographic orientation fibres and clustering the fibres based on a user-defined threshold (similar to defining a misorientation threshold in electron backscatter diffraction). The trial orientation clusters are tested and scored against the measured data, and all the orientations above a specified completeness threshold (expected peaks vs. measured peaks) are kept. These accepted orientations are sent to a fitting algorithm using a least-squares minimization to optimize the 12 grain parameters listed above. Uncertainties for ff-HEDM measurements are approximately 20 μm, 0.1°, and 10^{-4} for COM, orientation, and elastic strain respectively [31, 1].

Near-field HEDM

In the case of near-field HEDM (nf-HEDM) the detector is placed ∼5-10 mm away from the sample. Due to the proximity of the detector, the shapes of the diffraction peaks are the projections of the shapes of the diffracting grain (Fig. 3.1b). Reconstruction of this data gives grain morphology and orientation [50, 51, 52, 53, 54, 55]. The data in this work was reconstructed using a new algorithm where each voxel in the reconstruction was tested and scored against every orientation indexed in the ff-HEDM reconstruction. Only the orientations in the list were tested.

4.1.2 Ti-7Al

The Ti-7Al used in this work is a hexagonal close packed α-Ti alloy, and is similar to the α-phase in Ti-6Al-4V which is a commonly used alloy in the aerospace and biomedical industries. Ti-7Al is high strength with low stiffness and has large plastic anisotropy [56, 57], making it ideal for HEDM measurements, so a significant amount of work has been done on characterizing the deformation of Ti-7Al using HEDM [22, 23, 24, 25, 6, 26].

Plastic deformation in α-Ti is mainly occurs through the slip on the basal systems $\langle a \rangle$, $\langle 1\bar{2}10 \rangle \{0001\}$, and on the prismatic systems $\langle a \rangle$, $\langle 1\bar{2}10 \rangle \{10\bar{1}0\}$. Slip can also be observed on the pyramidal $\langle a \rangle$, $\langle 11\bar{2}0 \rangle \{1\bar{1}01\}$ slip systems but with lower frequency [56, 22, 6, 58, 42]. These families of slip systems have been shown vary significantly in strength [56, 6].

Aging of Ti-7Al leads to short-range ordering (SRO) and the development of coherent α_2 Ti_3Al nanoprecipitates, which affects the mechanical behavior of titanium alloys with greater than 5% aluminum [28]. The α_2 precipitates suppress twinning and amplify slip on the basal planes [29, 30]. The presence of SRO and α_2 precipitates also impedes dislocation motion, raising the slip system strength on the basal and prismatic planes. As slip occurs, dislocation motion shears these obstacles, which causes softening of the basal and prismatic slip systems with increasing macroscopic strain [6, 38].

The last family of slip systems is the pyramidal $\langle c+a \rangle$ where slip occurs through the glide of dislocations on the $\{10\bar{1}1\}$ and $\{11\bar{2}2\}$ plane families [59]. As plastic deformation occurs, the tangling of dislocations causes hardening on these planes [6]. As a consequence of the competing hardening and softening behaviors, Ti-7Al exhibits little to no hardening on a macroscopic level [6].

4.1.3 Spectral FFT-based Micromechanical Modeling

One method of full-field micromechanical modeling that is increasing in popularity due to its efficiency is a spectral FFT-based method [60, 61, 62, 63] where a grain map is used as the input. This work is being based on an elasto-viscoplastic FFT (evpFFT) formulation of this method. The local stress and strain fields are calculated at each voxel of the micostructure under the applied boundary conditions such that stress equilibrium and strain compatability are fulfilled. The evpFFT method makes a small strain assumption and used the constitutive equation:

$$\epsilon_{ij}(x) = \epsilon^e_{ij}(x) + \epsilon^p_{ij}(x) = C^{-1}_{ijkl}(x)\sigma_{kl}(x) + \epsilon^{p,t}_{ij} + \dot{\epsilon}^p_{ij}(x,\sigma)\Delta t \tag{4.9}$$

where $\epsilon_{ij}(x)$ is the local total strain, calculated as summation of the local elastic strain, $\epsilon^e_{ij}(x)$, and local plastic strain, $\epsilon^p_{ij}(x)$, all of which are solved at each point x. Elastic strain is computed via Hooke's law from the inner product of the stiffness matrix, $C^{-1}_{ijkl}(x)$, and the local stress, $\sigma_{kl}(x)$ at each point. Plastic strain is given as the accumulated plastic strain, $\epsilon^{p,t}_{ij}$, and the additional plastic strain from each increment, Δt, which is solved using an extended Voce hardening rule.

Since Ti-7Al is a hexagonal material, it has residual strains on the order of 10^{-3}, and it becomes necessary to consider these in the initial state of the micromechanical calculation. The residual strains measured from ff-HEDM are grain-averaged, and can be converted to eigenstrain using a method developed by Pokharel & Lebensohn [64]. The initial approximation is calculated using the Eshelby's approximation

$$\epsilon^{*(g)}_{ij} = (S - I)^{-1}_{ijkl}\epsilon^{e(g)}_{kl} \tag{4.10}$$

which treats a grain, g, as an ellipsoidal inclusion embedded in a homogeneous matrix. $\epsilon_{ij}^{*(g)}$ is the constant eigenstrain in the grain, $\epsilon_{kl}^{e(g)}$ is the resulting uniform elastic strain inside the inclusion, and S is the fourth-ranked Eshelby tensor.

However, the instantiation of eigenstrains by this method does not create a perfect correlation between measured and modeled elastic strains in grains, so a modification has to be made in the form of a symmetric matrix of six correction factors, $\beta_{ij} = 1/m_{ij}^{\epsilon}$, where m_{ij}^{ϵ} is the slope of the line of the correlation [64]. Thus the modified Eshelby's approximation is

$$\epsilon_{ij}^{*(g)} = \beta_{ij}(S - I)_{ijkl}^{-1}\epsilon_{kl}^{e(g)} \tag{4.11}$$

4.2 Experiment

4.2.1 Material

The Ti-7Al material used for this work, with nominal composition Ti-7.02Al-0.11O-0.015Fe (wt.%), was cast as an ingot and hot isostatic pressed to reduce porosity. Then it was extruded followed by annealing at 962°C for 24 hours before air cooling [34]. This processing produced sample with grain size in the approximate range of $30 - 400$ μm. The sample was cut using electrical discharge machining to minimize the introduction of additional residual stresses.

4.2.2 Experiment Description

A sample of Ti-7Al with the same geometry as the sample of interest was loaded in uniaxial tension. The macroscopic stress-strain curve (Fig. 4.3a) was calculated using digital image correlation (DIC) with the surface features created by the machining, and the yield strength was found to be approximately 610 N.

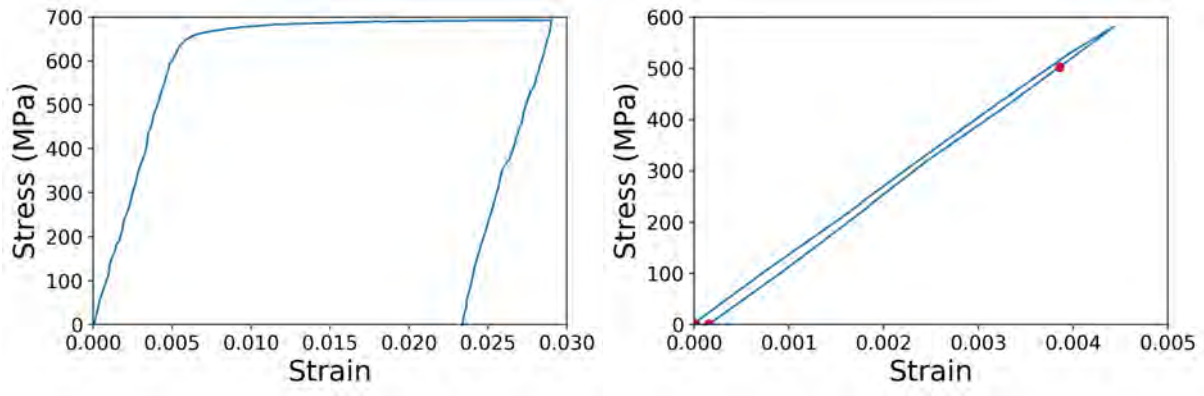

(a) (b)

Figure 4.3: (a) Stress-strain curve created by Ti-7Al tensile test with yield strength of 610 N. (b) The cyclic stress-strain curves were calculated using DIC for the first load cycles with the points marked where ff-HEDM scans were taken.

200 loading cycles to 550 N (∼90% of yield) were performed on a sample of Ti-7Al using the RAMS2 load frame [35] at the F2 beamline at the Cornell High Energy Synchrotron Source (CHESS). The sample had a gauge length of 8 mm and a 1 mm x

1 mm cross-sectional area. Tomography, nf-HEDM and ff-HEDM scans were taken in the initial unloaded state. Then, the sample was loaded to 550 N and unloaded to 475 N to minimize stress relaxation, and another ff-HEDM scan was taken over the same approximate volume. The sample was unloaded back to 0 N and a final ff-HEDM scan was taken (Fig. 4.3b). This process was repeated at cycles 2, 5, 10, 20, 30, and every 10 cycles until reaching a total of 200 cycles. The macroscopic stress-strain curves were calculated using DIC.

Both the nf-HEDM and ff-HEDM scans were taken for a full 360° at an ω interval of 0.25° using an energy of 61.332 keV. The nf-HEDM data was taken with five 220 μm tall "boxbeam" volumes (with an overlap of 10 μm on the top and bottom to account for slit scattering) to cover a 1 mm x 1 mm x 1 mm volume. This data was collected using a Lu:Ag ($Al_5Lu_3O_{12}$) scintillator with a Retiga 4000DC camera (2048 x 2048 pixels, 1.48 μm pixel size).

A 1.1 mm tall volume (with 50 μm on the top and bottom to allow for slit scattering) of ff-HEDM data was collected in six wedges of 60° with an x-ray attenuation of 7.75 mm of lead using a GE amorphous silicon area detector (2048 x 2048 pixels, 200 μm pixel size).

After the 200th cycle, a ff-HEDM scan was taken with 7 mm of lead attenuation to capture more diffraction from the smaller grains in order to index the sample better for the nf-HEDM reconstruction.

4.2.3 Data Processing

Far-field HEDM data

The ff-HEDM data was reduced using the HEXRD software package (`https://github.com/joelvbernier/hexrd`) [31]. The initial detector parameters were calibrated using a CeO_2 powder pattern to find the x-tilt, y-tilt, and distortions of the detector as well as estimating the location of the sample rotation axis. The grains in the Ti-7Al sample were indexed and fit to the last full ring on the detector using lattice parameters of $a = 2.9321$ Å and $c = 4.6843$ Å. Then, the detector calibration was finished using a high completeness grain close to the vertical center of the scanned volume.

After the detector was calibrated, the dataset was reduced using a 2θ max of 10. CHESS has a vertical beam energy gradient that produces a systematic error in the measured strain state which looks like a volumetric strain added onto the elastic strain tensor. In order to correct for this, the volumetric strain of each grain was plotted against the vertical component of its COM in the beam (Fig. 4.4). A line was fit to the data and the same amount was subtracted from each of the principal components to force the volumetric strain to zero. Then, this same volumetric strain was subtracted from each of the subsequent scans. All data in the top and bottom 50 μm was filtered out to account for slit scattering.

The final ff-HEDM scan was indexed and fit with 2θ max values of 7, 10, 12.5, and to the last full ring on the detector. Then these fits were stitched together in order to get the best fits on as many grains as possible. The more rings that are used to fit the grains, the better the fit, but small grains do not diffract as intensely as larger grains, so the higher order x-ray peaks are too weak to be picked up on the outer rings. This indexed data was then used to seed the nf-HEDM reconstruction.

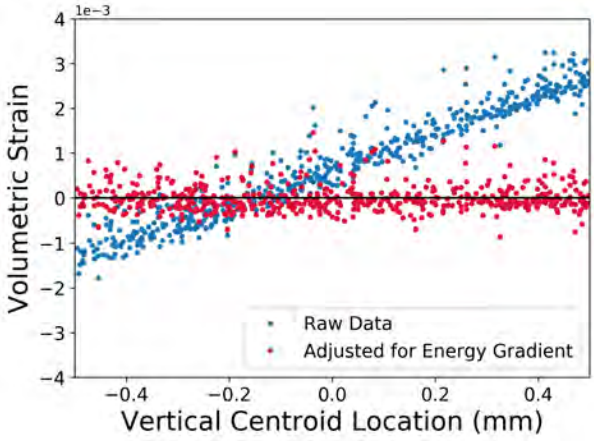

Figure 4.4: The x-ray beam at CHESS has an energy gradient which manifests as a volumetric strain through the height of the beam.

Near-field HEDM data

The nf-HEDM data was reconstructed using a HEXRD with a 5 μm vertical step size per layer and 5 μm resolution within the layer for 40 layers per scanned volume for a total of 200 layers. All of the data in the top and bottom 10 μm was omitted and not reconstructed to account for slit scattering. The layers of grain maps were read into and stacked using Dream.3D [65].

4.3 Results

The initial tomography reconstruction showed that the cross sectional area for the sample was $\sim$0.94 mm^2 (Fig. 4.5). This means when the sample was loaded, the macroscopic stress was actually 585 MPa and the loaded scans were taken at 505 MPa.

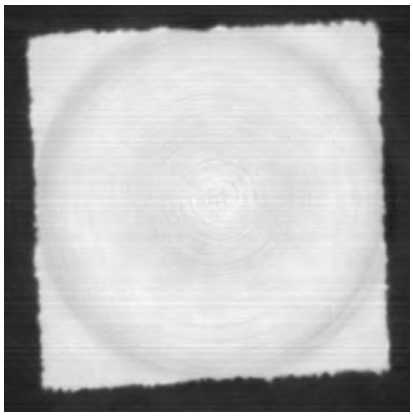

Figure 4.5: The tomography reconstruction revealed the sample had a cross sectional area of $\sim$0.94 mm^2.

The macroscopic stress-strain curve for the first cycle shows that some plasticity occurred, while the curve for the second cycle exhibits a stable elastic response that lies on top of the unloading of the first cycle (Fig. 4.6).

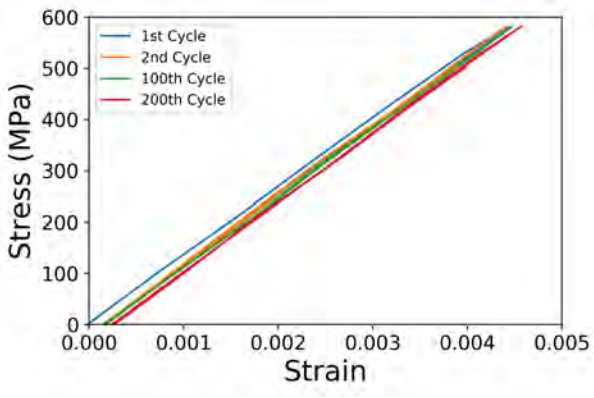

Figure 4.6: The unloading for the first cycle has shifted slightly from the loading for that cycle while the second cycle lands on top of the unloading cycle for the first cycle. By the 100th cycle, the curve has shifted just slightly more, and the 200th cycle has shifted even slightly more.

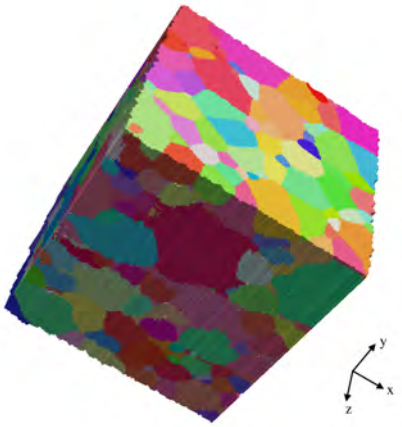

Figure 4.7: The nf-HEDM volume was reconstructed using HEXRD with no misorientation from the grain-averaged orientations found in the ff-HEDM data.

Within the 1 mm x 1 mm x 1 mm volume, 707 grains were found (Fig. 4.7), of which 553 were considered to be high fidelity ($\chi^2 > 2 \times 10^{-3}$).

Histograms were made to examine the distribution of strain in the loading direction at 0 load after varying numbers of cycles (Fig. 4.8). In the initial state, the peak of the distribution is not at 0. It is slightly negative, and the distribution is asymmetric. However, after the first cycle, the distribution shifts to symmetric and now peaks at 0. By the time we reach 200 cycles, the distribution has broadened out and is asymmetric again, but the peak of the distribution is still around 0.

This data for the initial change can also be analyzed using a normal probability plot where a straight line would represent a normal distribution (Fig. 4.9). While cycles 1, 2, and 5 appear to be reasonably approximated by the same distribution, the data for the initial state is significantly different. The tail on the initial distribution shows that about 15% of grains have an initial strain higher than expected by the bulk of the distribution. Additionally, the mean for the initial cycle has a higher compressive strain than the other states.

In order to probe this result further, histograms were made of each grain's change in

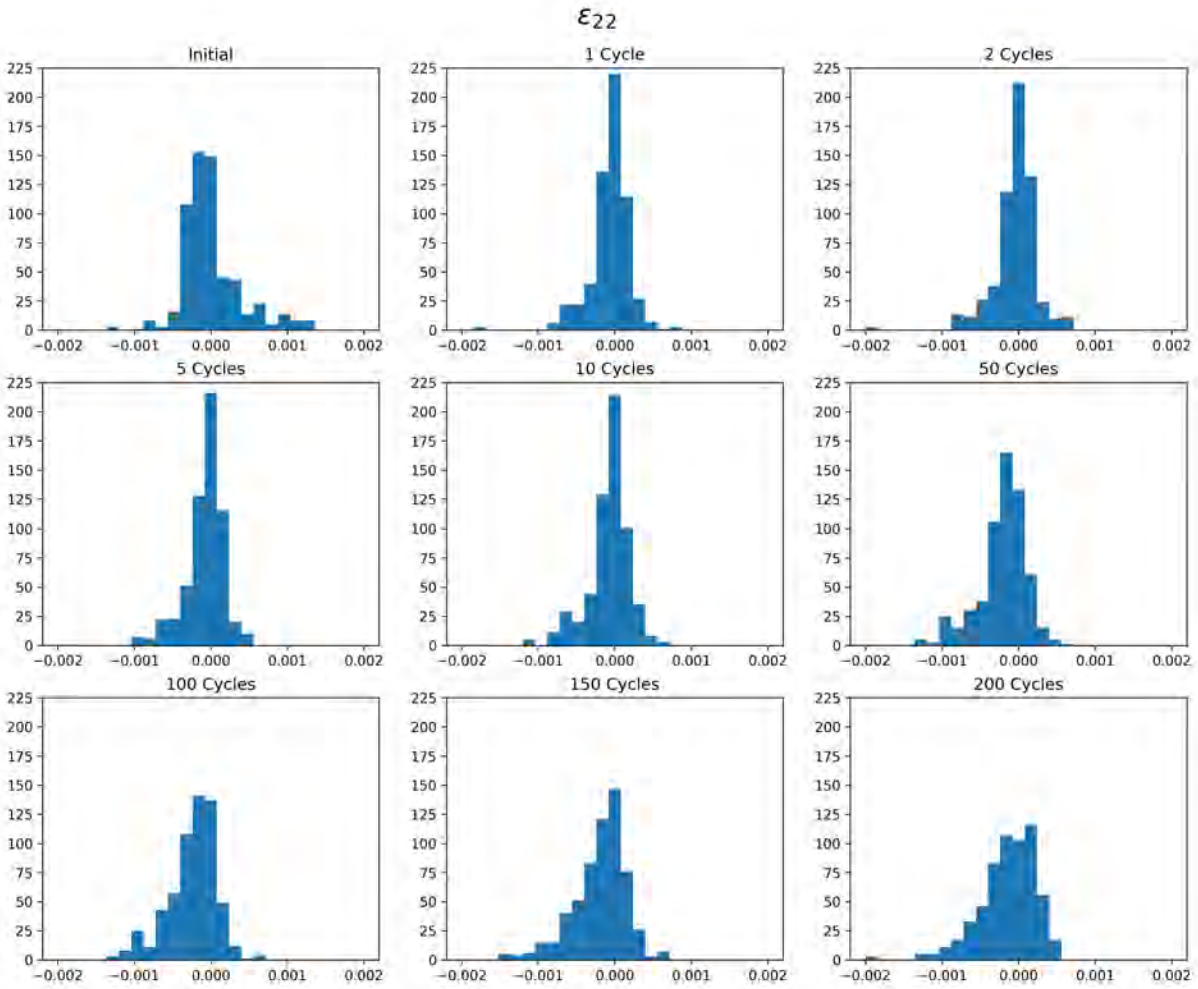

Figure 4.8: The distribution of ϵ_{22} in the initial state is significantly different from the distributions of strains after 1, 2, and 5 cycles respectively. Later cycles show a development of asymmetry in the distribution with the development of a tail in the negative direction.

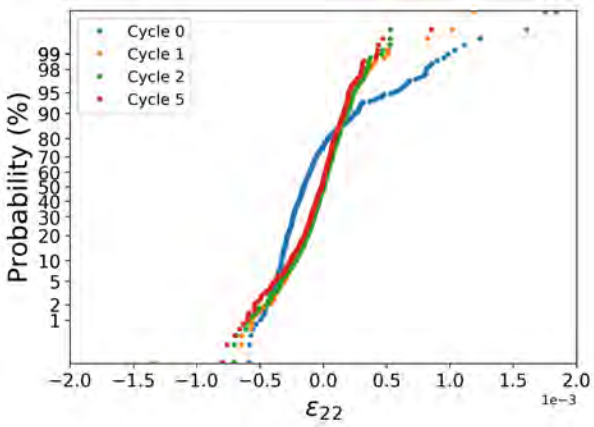

Figure 4.9: The normal probability distribution of ϵ_{22} shows a change in the distribution from the initial state to the states after 1, 2, and 5 cycles.

ϵ_{22}. There was a wide distribution of $\Delta\epsilon_{22}$ for the first loading cycle while the majority of grains exhibited very little change in ϵ_{22} over the second loading cycle (Fig. 4.10).

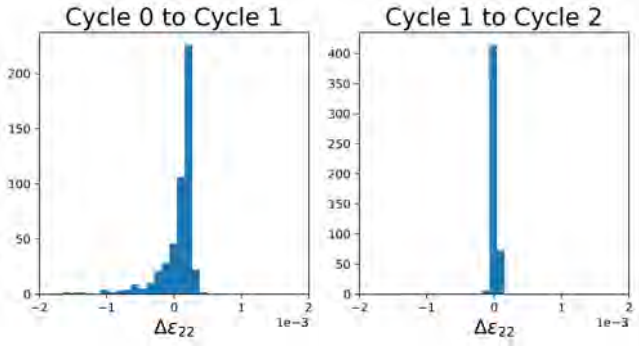

(a) (b)

Figure 4.10: During (a) the first cycle, there are more grains that have a non-negligible change in ϵ_{22} compared to (b) the second cycle.

Plotting $\Delta\epsilon_{22}$ vs. the initial ϵ_{22} for the ensemble of grains reveals a correlation between the original residual strain and the following change in strain in the loading direction. The correlation shows grains with higher residual strains had a larger change in strain which was roughly equivalent to the original strain.

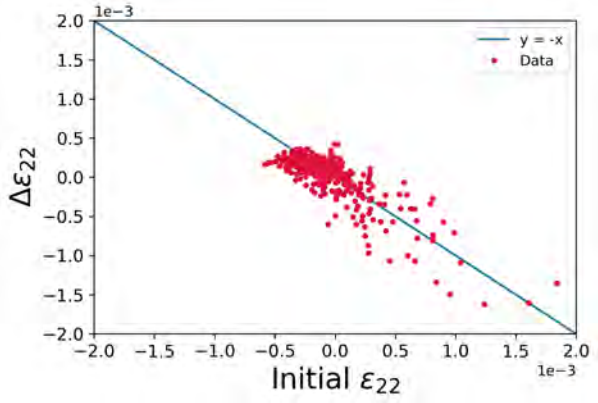

Figure 4.11: Points which land on the $y = -x$ line indicate a decrease in strain in the loading direction by the amount of initial residual strain in the loading direction.

Taking a look at the $\Delta\epsilon_{22}$ vs. Δ orientation 4.3, the two variables turn out to be fairly well correlated, which is useful in that, if the strain component parallel to the loading direction implies slip events then the latter should cause lattice rotation, which is indeed the case.

In the probability plots for the von Mises stress and strain distributions (Fig. 4.13), a straight line indicates a normal distribution. The line rotates through increasing cycles indicating that the distributions of von Mises stress and strain are broadening.

In addition to looking at von Mises stress, it is interesting to look at how the stress tensor for each grain compares to the macroscopic stress tensor. Stress coaxiality angle relates the stress state of an individual grain to the macroscopic applied load and can be calculated as:

$$\phi = \cos^{-1}\left(\frac{\sigma_{macro} : \sigma_{grain}}{\|\sigma_{macro}\|\|\sigma_{grain}\|}\right) \tag{4.12}$$

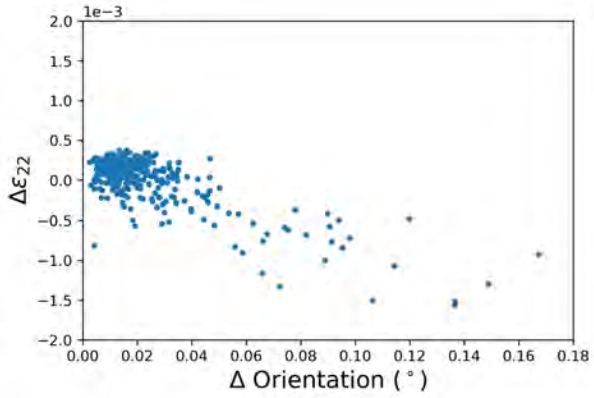

Figure 4.12: The grains with greater change in strain in the loading direction also had the greatest orientation change over the first cycle.

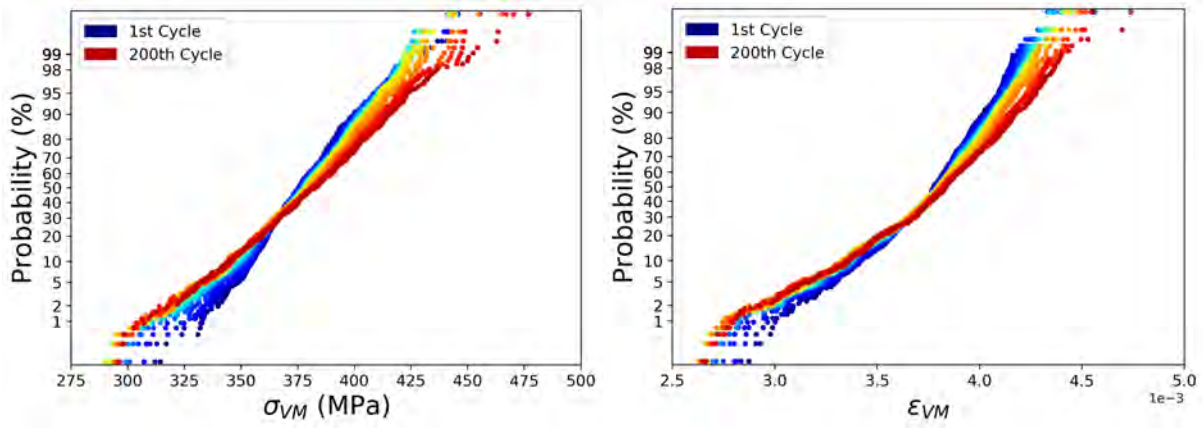

(a) (b)

Figure 4.13: Both the (a) von Mises stress and (b) von Mises strain show a rotation in the distribution around the 30% value suggesting that the distribution is spreading out (i.e. more high and low stress grains).

Schuren et al. [23] loaded a sample of Ti-7Al to close to the elastic limit, immediately released it to 473 MPa (which would be similar load history to our the initial scan of the sample being studied here), then held it at load for 24 hours. They showed that upon initial loading the hydrostatic tension decreases linearly with increasing stress coaxiality angle. However, in the sample being studied here, the opposite occurs, where the hydrostatic stress increases linearly with increasing stress coaxiality angle. When each successive state is graphed, however, around cycles 60-70 the trend changes towards closer to what Schuren et al. saw. By the time cycle 200 is reached, there is a similar shape to the post-creep state. One possible reason for the discrepancy in the initial state is the data used by Schuren et al. was one cross-section averaged scan rather than a full grain averaged volume.

The coaxiality angle can also be calculated with respect to each grains' initial stress state, rather than the macroscopic applied stress:

$$\phi = \cos^{-1}\left(\frac{\sigma^0_{grain} : \sigma_{grain}}{\|\sigma^0_{grain}\|\|\sigma_{grain}\|}\right) \tag{4.13}$$

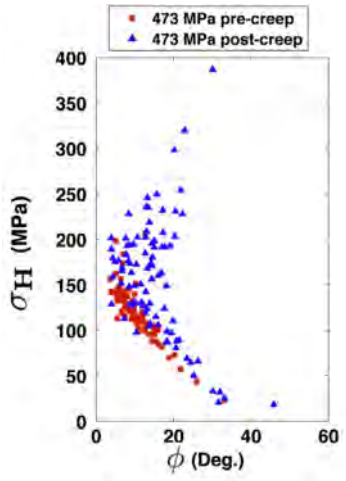

Figure 4.14: Schuren et al. showed in the initial loading condition, hydrostatic stress decreased linearly with stress coaxiality angle.

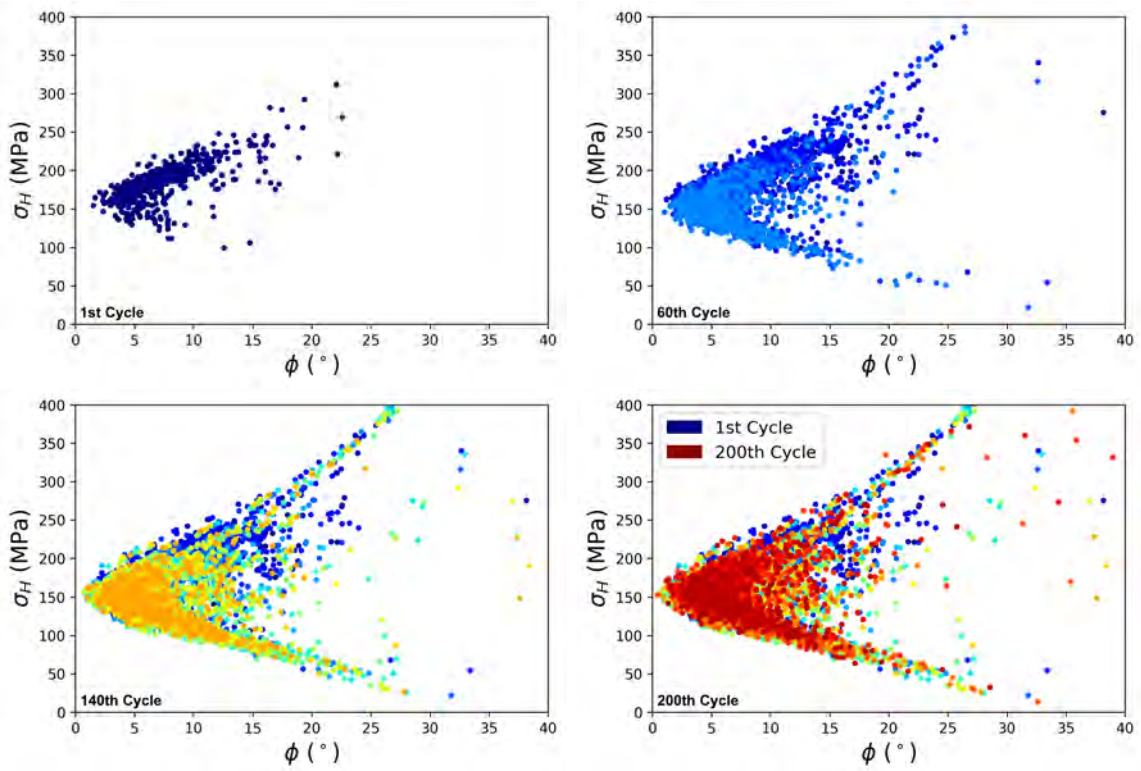

Figure 4.15: In the sample being studied here, the initial loaded state shows the opposite trend to Schuren et al. with a rotation after 60-70 cycles towards the trend they saw. By the 200th cycle, the trend matches their post-creep data point.

The distribution of the coaxiality angle with respect to each grains' initial stress state gets larger with increasing cycles (Fig. 4.16, which suggests that as the number of cycles increases, the stress tensor of each grain becomes less aligned with its original stress tensor.

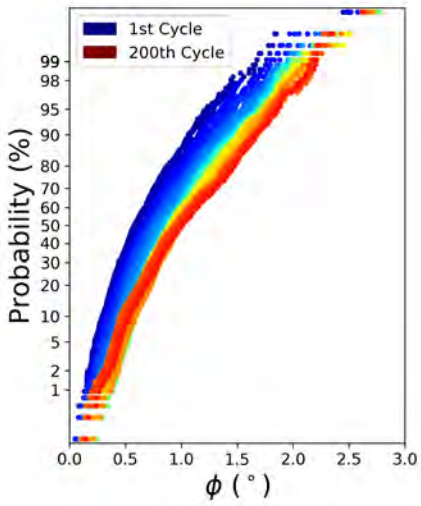

Figure 4.16: The distribution of coaxiality angles calculated with respect to the initial grain stress tensor broadens through increasing cycles.

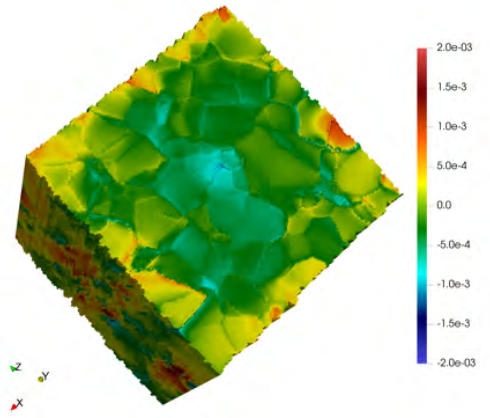

Figure 4.17: The initial elastic strain field in the loading direction was calculated from the eigenstrain using evpFFT.

4.4 Modeling

The FF data was used along with the NF grain map to initialize the model using Eshelby's approximation (Eq. 4.10). This instantiation was put into evpFFT where the elastic strain field was calculated (Fig. 4.4, then the elastic strain tensor was averaged across each grain and compared with the measured elastic strain tensor (Fig. 4.4a). β_{ij} was calculated from the slopes of the regression line with respect to y=x. The initial elastic strain was recalculated and gave better correlations than without β_{ij} (Fig. 4.4b). The micromechanical model was run for one loading cycle (Fig. 4.4) and the calculated strains were compared with the measured strains (Fig. 4.4). Five of the six strain tensor components correlate well between the measured and modeled data after one cycle, and the strain in the loading direction is the component that does not match.

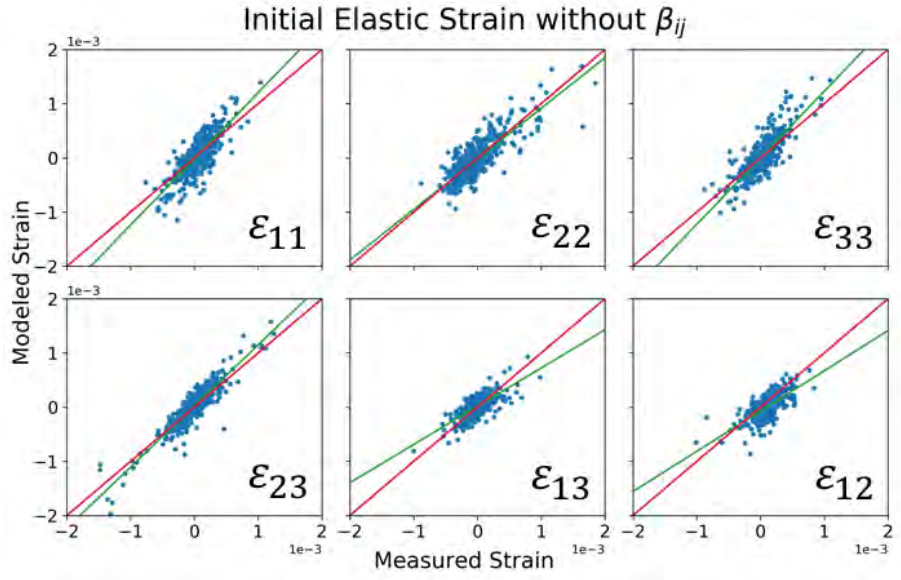

(a)

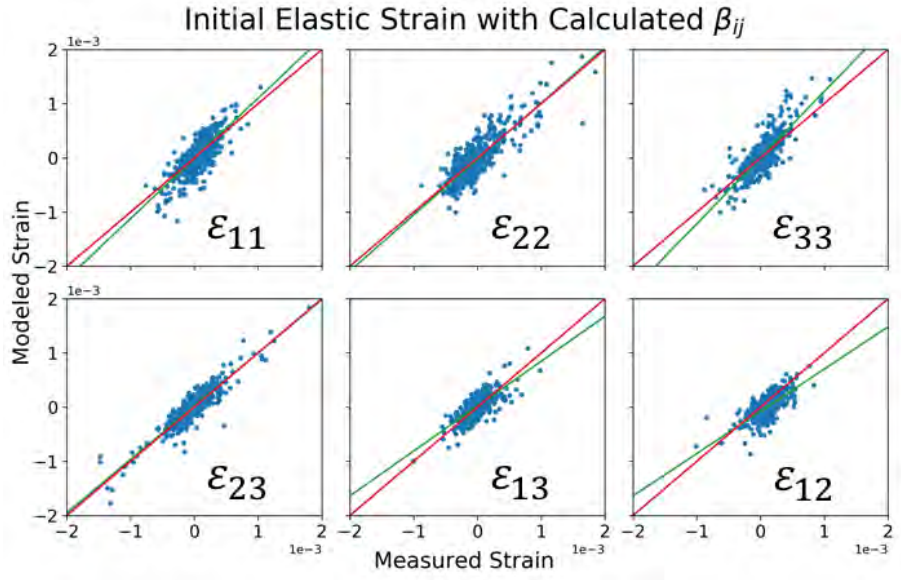

(b)

Figure 4.18: The correlations between modeled and measured strain are better after calculating the β_{ij}.

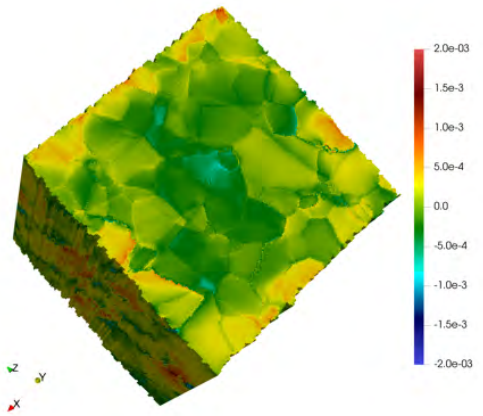

Figure 4.19: The elastic strain field in the loading direction after the first cycle calculated using evpFFT.

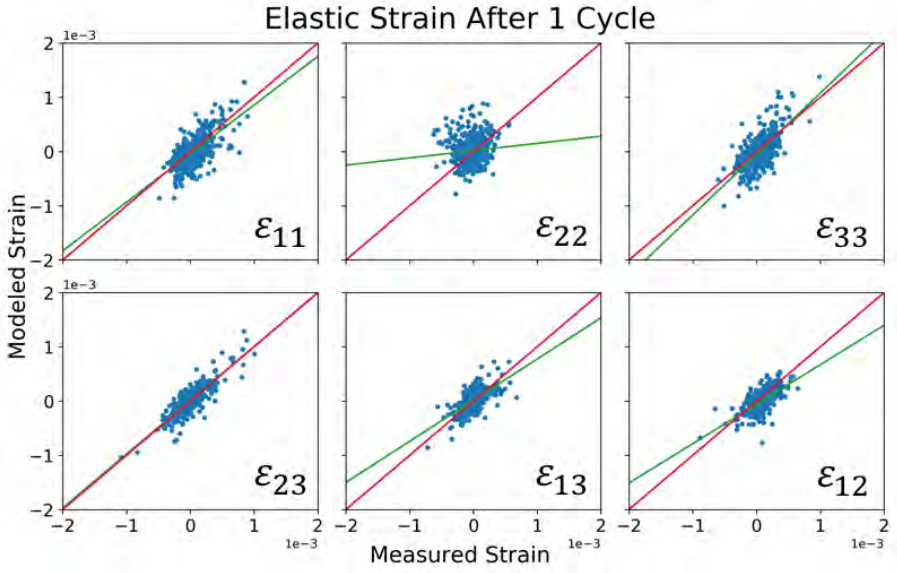

Figure 4.20: All of the strain tensor components match reasonably well except for in the loading direction.

4.5 Discussion

"Boxbeam" nf-HEDM is still very much in development as well as nf-HEDM data reconstruction using HEXRD. Currently, HEXRD only performs a near field-HEDM reconstruction of a 3D polycrystal with the list of orientations previously found in the far field-HEDM reconstruction. This means that, if an orientation cluster is missing from the ff-HEDM results, it will also be missing from the nf-HEDM reconstruction. Also, the nf-HEDM data will only be reconstructed using the grain-averaged orientation unless the program is specifically told to reconstruct with misorientation allowed between the grain average and each individual voxel, which is significantly slower. One nf-HEDM reconstruction (40 layers) will take about two hours to finish on a 32 core workstation with no misorientation specified, but will take closer to 72 hours for two misorientation steps. This approach can be contrasted with the "traditional" nf-HEDM method that uses a line-focused beam and layer-wise reconstruction in which each voxel is, in principle, independently reconstructed thus allowing for the substantial orientation gradients found in plastically deformed material. Nevertheless, the boxbeam approach enables efficient non-destructive reconstruction of a 3D polycrystal with elastic strain. The results presented here demonstrate the utility of applying the methods for investigating the response to cyclic loading in a polycrystalline sample of Ti-7Al.

4.6 Conclusion

An experiment was conducted at CHESS in which a polycrystalline sample of Ti-7Al was cyclically deformed and mapped using boxbeam nf-HEDM and ff-HEDM. The ff-HEDM shows a decrease in residual elastic strain over the first cycle followed by an increasing build-up of strain. The initial residual strain in each grain was anti-correlated with the change in that same strain component over the first cycle. However, the mechanism for this drop in residual strain has not yet been identified. The distribution in the von Mises stress and von Mises strain, which are scalar measures of shear stresses and strains, broaden with increasing cycles. Initially, a graph of hydrostatic stress against stress coaxiality angle shows a positive correlation but after about 65 cycles, the trendline has rotated to a negative correlation. By cycle 200, the hydrostatic stress vs. stress coaxiality angle is a scatter plot with no obvious trend.

The modeling of the experiment was started using a spectral FFT-based micromechanical model, and using a modified Eshelby's approximation leads to better correlations between measured and modeled elastic strain values. After the first cycle, the modeled values of elastic strain reasonably match those of measured experimentally except for the strain in the loading direction. This is likely due to the need for a better plasticity model.

References

[1] J. K. Edmiston, N. R. Barton, J. V. Bernier, C. Johnson, D. J. Steigmann, Precision of lattice strain and orientation measurements using high-energy monochromatic X-ray diffraction research papers, Journal of Applied Crystallography 44 (2011) 299–312.

[2] H. W. Coleman, W. G. Steele, Experimentation, validation, and uncertainty analysis for engineers, 3rd Edition, Wiley, Hoboken, NJ, 2009.

[3] J. C. Schuren, M. P. Miller, Quantifying the uncertainty of synchrotron-based lattice strain measurements, Journal of Strain Analysis for Engineering Design 46 (7) (2011) 663–681.

[4] L. Renversade, A. Borbély, Evaluation of grain-average stress tensor in a tensile-deformed Al-Mn polycrystal by high-energy X-ray diffraction, Journal of Applied Crystallography 50 (2017) 1144–1157.

[5] T. Kanit, S. Forest, I. Galliet, V. Mounoury, D. Jeulin, Determination of the size of the representative volume element for random composites: Statistical and numerical approach, International Journal of Solids and Structures 40 (13-14) (2003) 3647–3679. doi:10.1016/S0020-7683(03)00143-4.

[6] D. C. Pagan, P. A. Shade, N. R. Barton, J. S. Park, P. Kenesei, D. B. Menasche, J. V. Bernier, Modeling slip system strength evolution in Ti-7Al informed by in-situ grain stress measurements, Acta Materialia 128 (2017) 406–417.

[7] P. Kesavan Nair, R. Vasudevan, Residual stresses of types II and III and their estimation, Sadhana 20 (1) (1995) 39–52.

[8] J. L. Warwick, J. Coakley, S. L. Raghunathan, R. J. Talling, D. Dye, Effect of texture on load partitioning in Ti-6Al-4V, Acta Materialia 60 (10) (2012) 4117–4127.

[9] Z. Zheng, P. Eisenlohr, T. R. Bieler, D. C. Pagan, F. P. E. Dunne, Heterogeneous Internal Strain Evolution in Commercial Purity Titanium Due to Anisotropic Coefficients of Thermal Expansion, JOM.

[10] R. R. Pawar, V. T. Deshpande, The anisotropy of the thermal expansion of a-titanium, Acta Crystallographica 24 (1968) 316–317.

[11] H.-D. Erfling, Studien zur thermischen ausdehnung fester stoffe in tiefer temperatur. iii (Ca, Nb, Th, V, Si, Ti, Zr), Annalen der Physik 433 (6) (1942) 467–475.

[12] E. S. Greiner, W. C. Ellis, Thermal and Electrical Properties of Ductile Titanium, Transactions of the American Institute of Mining and Metallurgical Engineers 185 (5) (1949) 335–336.

[13] C. J. McHargue, J. P. Hammond, Deformation Mechanisms in Titanium at Elevated Temperatures, Acta Metallurgica 1 (6) (1953) 700–701, 703–705.

[14] R. Berry, G. Raynor, A note on the lattice spacings of titanium at elevated temperatures, Research 6 (1953) 21s–23s.

[15] J. Spreadborough, J. W. Christian, The measurement of the lattice expansions and Debye temperatures of titanium and silver by x-ray methods, Proc. Phys. Soc 74 (1959) 609–615.

[16] W. T. Roberts, Preferred orientation and anisotropy in titanium, Journal of The Less-Common Metals 4 (1962) 345–361.

[17] R. H. Willens, Vacuum x-ray diffractometer for high temperature studies of metals sensitive to contamination by oxygen and nitrogen, Review of Scientific Instruments 33 (1962) 1069–1076.

[18] Y. Touloukian, R. Kirby, R. Taylor, P. Desai, Thermophysical properties of matter–the tprc data series. volume 12. thermal expansion metallic elements and alloys, Tech. rep., Thermophysical and Electronic Properties Information Analysis Center ... (1975).

[19] ASM International, Thermal Properties of Metals, ASM Ready Reference (2002) 5–7.

[20] J. Boab, R. W. K. Honeycombe, Thermal Fatigue of Metals, Nature 153 (3886) (1944) 494.

[21] A. M. Russell, B. A. Cook, Coefficient of thermal expansion anisotropy and texture effects in ultra-thin titanium sheet, Scripta Materialia 37 (1997) 1461–1467.

[22] U. Lienert, M. C. Brandes, J. V. Bernier, J. Weiss, S. D. Shastri, M. J. Mills, M. P. Miller, In situ single-grain peak profile measurements on Ti – 7Al during tensile deformation, Materials Science and Engineering A 524 (2009) 46–54.

[23] J. C. Schuren, P. A. Shade, J. V. Bernier, S. F. Li, B. Blank, J. Lind, P. Kenesei, U. Lienert, R. M. Suter, T. J. Turner, D. M. Dimiduk, J. Almer, New opportunities for quantitative tracking of polycrystal responses in three dimensions, Current Opinion in Solid State and Materials Science 19 (2015) 235–244.

[24] K. Chatterjee, A. Venkataraman, T. Garbaciak, J. Rotella, M. D. Sangid, A. J. Beaudoin, P. Kenesei, J. S. Park, A. L. Pilchak, Study of grain-level deformation and residual stresses in Ti-7Al under combined bending and tension using high energy diffraction microscopy (HEDM), International Journal of Solids and Structures 94-95 (2015) 35–49.

[25] T. J. Turner, P. A. Shade, J. V. Bernier, S. F. Li, J. C. Schuren, P. Kenesei, R. M. Suter, J. Almer, Crystal plasticity model validation using combined high-energy diffraction microscopy data for a Ti-7Al specimen, Metallurgical and Materials Transactions A 48 (2017) 627–647.

[26] D. C. Pagan, J. V. Bernier, D. Dale, J. P. Ko, T. J. Turner, B. Blank, P. A. Shade, Measuring Ti-7Al slip system strengths at elevated temperature using high-energy X-ray diffraction, Scripta Materialia 142 (2018) 96–100.

[27] A. Van de Walle, M. Asta, First-principles investigation of perfect and diffuse antiphase boundaries in HCP based Ti-Al alloys, Metallurgical and Materials Transactions A 33 (2002) 735–741.

[28] A. Venkataraman, P. A. Shade, R. Adebisi, S. Sathish, A. L. Pilchak, G. B. Viswanathan, M. C. Brandes, M. J. Mills, M. D. Sangid, Study of structure and deformation pathways in Ti-7Al using atomistic simulations, experiments, and characterization, Metallurgical and Materials Transactions A 48 (2017) 2222–2236.

[29] A. Fitzner, J. Quinta da Fonseca, J. Kelleher, M. Pascal, D. G. L. Prakash, M. Thomas, S.-Y. Zhang, M. Preuss, The effect of aluminium on twin activity in binary α-Ti, Acta Materialia 103 (2016) 341–351.

[30] T. Neeraj, M. J. Mills, Short-range order (SRO) and its effect on the primary creep behavior of a Ti - 6wt.% Al alloy, Materials Science & Engineering A 321 (2001) 415–419.

[31] J. V. Bernier, N. R. Barton, U. Lienert, M. P. Miller, Far-field high-energy diffraction microscopy: a tool for intergranular orientation and strain analysis, The Journal of Strain Analysis for Engineering Design 46 (2011) 527–547.

[32] J. Oddershede, S. Schmidt, H. F. Poulsen, H. O. Sørensen, J. Wright, W. Reimers, Determining grain resolved stresses in polycrystalline materials using three-dimensional X-ray diffraction, Journal of Applied Crystallography 43 (2010) 539–549.

[33] J. Bernier, R. Suter, A. D. Rollett, J. Almer, High energy diffraction microscopy in materials science, Annual Reviews in Materials Research.

[34] A. L. Pilchak, Fatigue crack growth rates in alpha titanium: faceted vs. striation growth, Scripta Materialia 68 (2013) 277–280.

[35] P. A. Shade, B. Blank, J. C. Schuren, T. J. Turner, P. Kenesei, K. Goetze, R. M. Suter, J. V. Bernier, S. F. Li, J. Lind, U. Lienert, J. Almer, A rotational and axial motion system load frame insert for in situ high energy x-ray studies, Review of Scientific Instruments 86 (2015) 093902.

[36] V. Tari, R. A. Lebensohn, R. Pokharel, T. J. Turner, P. A. Shade, J. V. Bernier, A. D. Rollett, Validation of micro-mechanical FFT-based simulations using High Energy Diffraction Microscopy on Ti-7Al, Acta Materialia 154 (2018) 273–283.

[37] E. S. Fisher, C. J. Renken, Single-crystal elastic moduli and the hcp - bcc transformation in Ti, Zr, and Hf, Physical Review 135 (2A).

[38] M. J. Blackburn, J. C. Williams, Strength, deformation modes and fracture in titanium-aluminum alloys, ASM Transactions Quarterly 62 (1969) 398–409.

[39] L. J. Swartzendruber, L. H. Bennett, L. K. Ives, R. D. Shull, The TiAl phase diagram: the α-α2 phase boundary, Materials Science and Engineering 51 (1). doi:10.1016/0025-5416(81)90115-4.

[40] T. K. G. Namboodhiri, C. J. Mcmahon, H. Herman, Decomposition of the a-Phase in Titanium-Rich Ti-AI Alloys, Metallurgical Transactions 4 (1973) 1323–1331.

[41] T. K. Namboodhiri, On the TiAl phase diagram, Materials Science and Engineering 57 (1) (1983) 21–22. doi:10.1016/0025-5416(83)90022-8.

[42] J. C. Williams, R. G. Baggerly, N. E. Paton, Deformation behavior of hcp Ti-Al alloy single crystals, Metallurgical and Materials Transactions A 33 (2002) 837–850.

[43] E. Charkaluk, A. Constantinescu, H. Maitournam, K. Dang Van, Revisiting the Dang Van criterion, Procedia Engineering 1 (2009) 143–146.

[44] K. Dang Van, I. Papadopoulus, High-cycle metal fatigue: From theory to applications (1999).

[45] A. Constantinescu, K. Dang Van, M. H. Maitournam, A unified approach for high and low cycle fatigue based on shakedown concepts, Fatigue & Fracture of Engineering Materials & Structures 26 (2003) 561–568.

[46] R. J. Neustadt, F. W. Cagle, J. Waser, Vector algebra and the relations between direct and reciprocal lattice quantities, Acta Crystallographica 24 (1968) 247–248.

[47] J. V. Bernier, A general geometric model for parameterizing diffraction measurements, (unpublished).

[48] J. Oddershede, S. Schmidt, M. K. A. Koker, D. S. Dale, Near-field mapping with box beam using FABLE and GrainSweeper.3D (2016).
URL `http://www.chess.cornell.edu/software/anaconda/GrainMapping_instructions.pdf`

[49] M. Obstalecki, S. L. Wong, P. R. Dawson, M. P. Miller, Quantitative analysis of crystal scale deformation heterogeneity during cyclic plasticity using high-energy X-ray diffraction and finite-element simulation, Acta Materialia 75 (2014) 259–272.

[50] H. F. Poulsen, S. F. Nielsen, E. M. Lauridsen, S. Schmidt, R. M. Suter, U. Lienert, L. Margulies, T. Lorentzen, D. Juul Jensen, Three-dimensional maps of grain boundaries and the stress state of individual grains in polycrystals and powders, Journal of Applied Crystallography 34 (2001) 751–756.

[51] R. M. Suter, D. Hennessy, C. Xiao, U. Lienert, Forward modeling method for microstructure reconstruction using x-ray diffraction microscopy: Single-crystal verification, Review of Scientific Instruments 77 (2006) 1–12.

[52] U. Lienert, J. Almer, B. Jakobsen, W. Pantleon, H. F. Poulsen, D. Hennessy, C. Xiao, R. M. Suter, 3-dimensional characterization of polycrystalline bulk materials using high-energy synchrotron radiation, Materials Science Forum 539-543 (2007) 2353–2358.

[53] C. M. Hefferan, S. F. Li, J. Lind, U. Lienert, A. D. Rollett, P. Wynblatt, R. M. Suter, Statistics of high purity nickel microstructure from high energy x-ray diffraction microscopy, Computers, Materials, & Continua 14 (2009) 209–219.

[54] S. F. Li, J. Lind, C. M. Hefferan, R. Pokharel, U. Lienert, A. D. Rollett, R. M. Suter, Three-dimensional plastic response in polycrystalline copper via near-field high-energy X-ray diffraction microscopy, Journal of Applied Crystallography 45 (2012) 1098–1108.

[55] S. F. Li, R. M. Suter, Adaptive reconstruction method for three-dimensional orientation imaging, Journal of Applied Crystallography 46 (2013) 512–524.

[56] G. Lutjering, J. C. Williams, Titanium, 2nd Edition, Springer-Verlag, 2007.

[57] D. Tromans, Elastic anisotropy of hcp metal crystals and polycrystals, International Journal of Recent Research and Applied Studies 6 (2011) 462–483.

[58] X. Tan, H. Gu, C. Laird, N. D. H. Munroe, Cyclic deformation behavior of high-purity titanium single crystals: Part I. Orientation dependence of stress-strain response, Metallurgical and Materials Transactions A 29 (1998) 507–512.

[59] J. C. Williams, M. J. Blackburn, The identification of a non-basal slip vector in titanium and titanium-aluminum alloys, Physica Status Solidi 25 (1968) K1–K3.

[60] H. Moulinec, P. Suquet, A numerical method for computing the overall response of nonlinear composites with complex microstructure, Computer Methods in Applied Mechanics and Engineering 157 (1998) 69–94.

[61] R. A. Lebensohn, R. Brenner, O. Castelnau, A. D. Rollett, Orientation image-based micromechanical modelling of subgrain texture evolution in polycrystalline copper, Acta Materialia 56 (2008) 3914–3926.

[62] R. A. Lebensohn, A. K. Kanjarla, P. Eisenlohr, An elasto-viscoplastic formulation based on fast Fourier transforms for the prediction of micromechanical fields in polycrystalline materials, International Journal of Plasticity 32-33 (2012) 59–69.

[63] B. S. Anglin, R. A. Lebensohn, A. D. Rollett, Validation of a numerical method based on Fast Fourier Transforms for heterogeneous thermoelastic materials by comparison with analytical solutions, Computational Materials Science 87 (2014) 209–217.

[64] R. Pokharel, R. A. Lebensohn, Instantiation of crystal plasticity simulations for micromechanical modelling with direct input from microstructural data collected at light sources, Scripta Materialia 132 (2017) 73–77.

[65] M. A. Groeber, M. A. Jackson, DREAM.3D: A Digital Representation Environment for the Analysis of Microstructure in 3D, Integrating Materials and Manufacturing Innovation 3 (2014) 5.